Inhibitory circuits control leg movements during *Drosophila* grooming

Durafshan Sakeena Syed[1,*], Primoz Ravbar[1], Julie H. Simpson[1,2,*]

[1]Neuroscience Research Institute and Department of Molecular, Cellular and Developmental Biology, University of California, Santa Barbara, Santa Barbara, CA, USA

[2] Lead Contact

*Correspondence: dsakeena@gmail.com (D.S.S.), jhsimpson@ucsb.edu (J.H.S.)

ABSTRACT

Limbs execute diverse actions coordinated by the nervous system through multiple motor programs. The basic architecture of motor neurons that activate muscles which articulate joints for antagonistic flexion and extension movements is conserved from flies to vertebrates. While excitatory premotor circuits are expected to establish sets of leg motor neurons that work together, our study uncovered an instructive role for inhibitory circuits — including their ability to generate rhythmic leg movements. Using electron microscopy data in the *Drosophila* nerve cord, we categorized ~120 GABAergic inhibitory neurons from the 13A and 13B hemilineages into classes based on similarities in morphology and connectivity. By mapping their connections, we uncovered pathways for inhibiting specific groups of motor neurons, disinhibiting antagonistic counterparts, and inducing alternation between flexion and extension. We tested the function of specific inhibitory neurons through optogenetic activation and silencing, using high resolution quantitative analysis of leg movements during grooming. We combined findings from anatomical and behavioral analyses to construct a computational model that can reproduce major aspects of the observed behavior, demonstrating that these premotor inhibitory circuits can generate rhythmic leg movements.

Keywords: inhibition, motor control, rhythm, premotor, GABA, muscle synergy, limb coordination, connectome

GRAPHICAL ABSTRACT

Inhibitory connections define muscle synergies

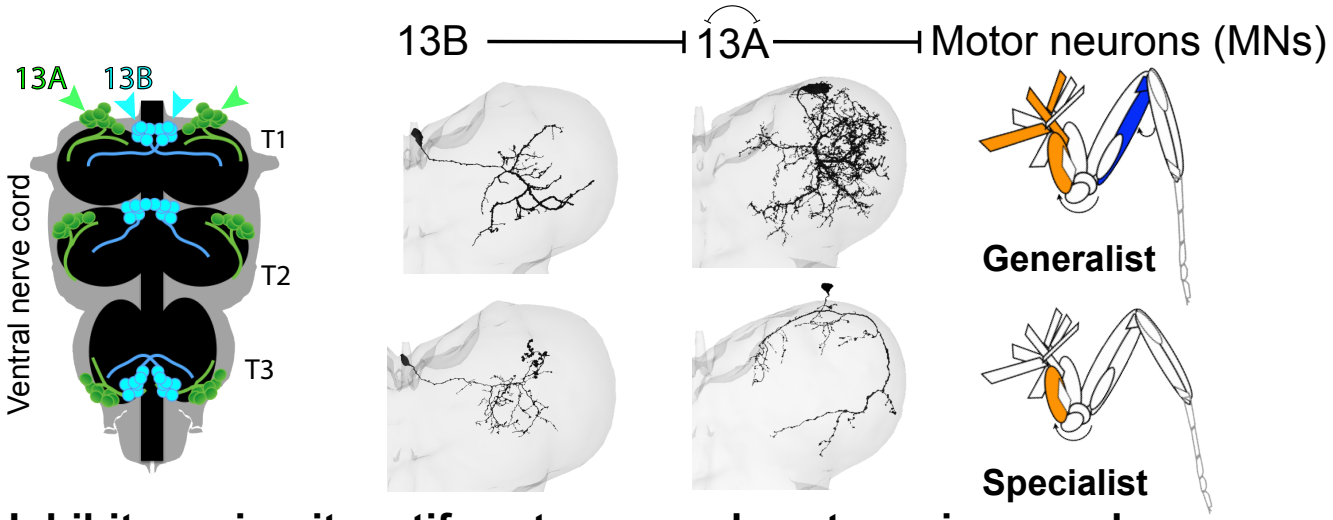

Inhibitory circuit motifs set up muscle antagonisms and extensor/flexor alternation

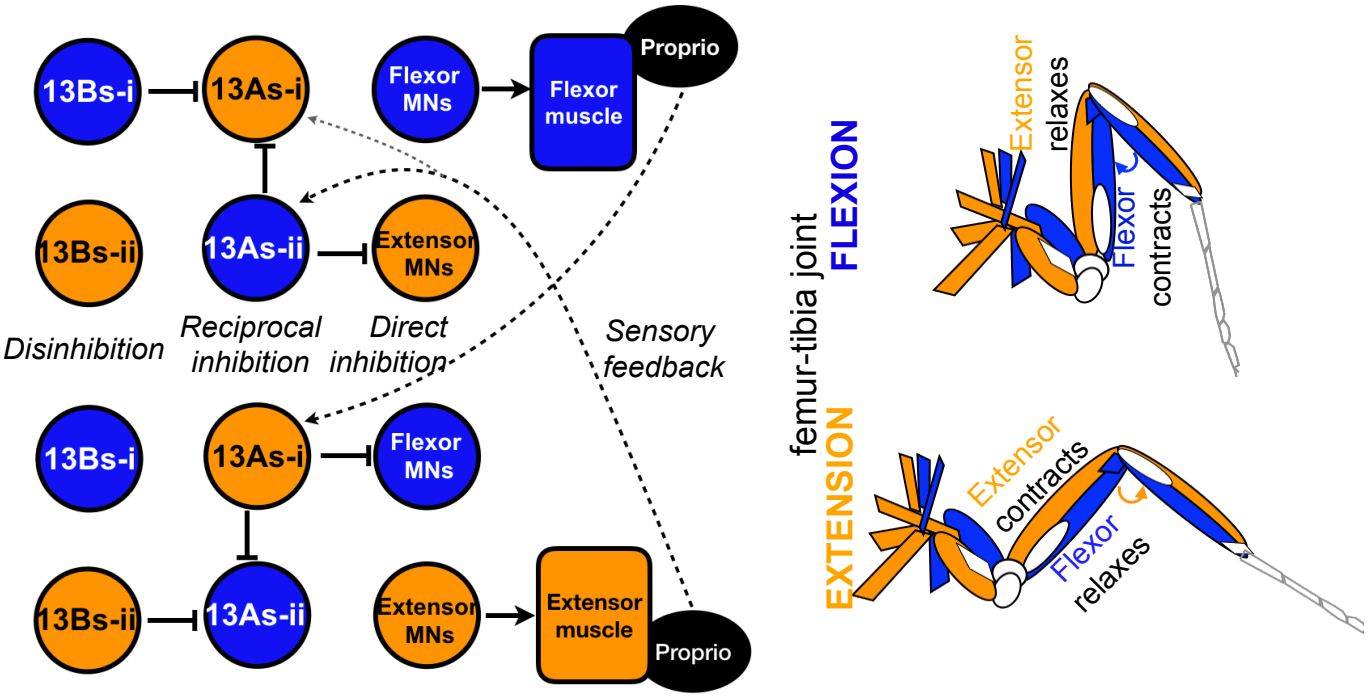

INTRODUCTION

All animals with limbs face the challenge of coordinating their movements to achieve precise motor control. Despite a limited set of muscles in each limb, the nervous system produces multiple flexible actions to generate behavior. These movements rely on a balance of inhibition and excitation, though the specific circuitry remains unclear. In various insects, coordinated leg movements have been studied extensively during walking and grooming, revealing both the flexibility and stereotypy of action sequences [1,2,3,4,5]. These studies highlight how insects provide a powerful system to understand the circuit basis of limb coordination. *Drosophila* grooming involves coordinated, rhythmic leg movements to sweep the body and remove debris[6] with different actions prioritized sequentially. While sensory, command-like, and motor neurons (MNs) are known components of grooming circuits[7,8,9,10,11,12,13], the contribution of GABAergic inhibitory neurons has not been systematically investigated. We hypothesize that these neurons contribute to limb coordination and subroutine selection.

Leg movements during grooming require precise flexor-extensor coordination, controlled by MNs and premotor circuits. Flies use 14 intrinsic leg muscles and 3-5 body wall muscles[14,15,16], organized into antagonistic pairs. Around 70 excitatory MNs innervate these muscles[16,17,18,19,20] and recent connectomic mapping has revealed premotor neurons in the ventral cord neuromeres associated with each leg[21,22]. The are around 622 local premotor interneurons[21], suggesting complex control architectures. Studies in stick insects, locusts, cockroaches, and crustaceans, have also revealed large numbers of interconnected pre-motor interneurons, some of which constitute central pattern generator circuits that shape rhythmic movements and interlimb coordination[5,23,24,25,26,27,28,29,30,31,32,33]. In *Drosophila* larvae, circuits containing both excitatory and inhibitory interneurons generate rhythmic muscle contractions within segments and propagate peristaltic waves between segments for crawling[34,35,36,37,38,39]. Together, these findings support the idea that premotor neurons may be a core component for generating and coordinating rhythmic motor control.

We investigate the role of inhibitory neurons in coordinating which leg muscles in adult *Drosophila* work together or antagonistically, and how they might produce rhythmic alternations. Neurons from a given lineage usually share a neurotransmitter, and there are 12 GABAergic hemilineages present in the ventral nerve cord (VNC)[40]. We identified neurons from GABAergic 13A and 13B hemilineages in a behavioral screen for grooming defects. Approximately 67±6 13A neurons and 47±1 13B neurons have been reported per hemisegment[40,41]. While activating all 13B and some 13A neurons induces leg extensions[40,42], further investigation is required to understand specific role of different subsets in leg coordination. The role of 13A neurons has been unclear due to the lack of tools for exclusive genetic labeling.

Since grooming and walking[43] require leg movements, we expect neural control circuits to overlap, particularly in flexion-extension alternation. MNs controlling similar muscles within a joint receive similar premotor inputs[21]. Descending neurons hypothesized to be involved in walking synapse onto premotor inhibitory neurons from several lineages[22].

These central circuits also receive sensory feedback from leg proprioceptors[44,45,46,47]. Recent connectome mapping and genetic tools provide opportunities to test how central and peripheral signals coordinate limb movement.

Muscle synergies describe groups of co-activated muscles, while motor primitives are elemental movement patterns that serve as building blocks of behavior[48,49]. Micro-stimulation of specific spinal cord regions in vertebrate models induced coordinated muscle contractions[50,51,52,53,54,55,56], with co-stimulation leading to combinations of contractions, indicating how coordinated regulation by premotor circuits can simplify assembly of more complex movements[49,56,57,58]. Additional evidence for synergies comes from electromyography, kinematics, neural recordings and computational modeling[59,60,61,62,63,64,65,66,67]. In vertebrates, the neural circuits responsible for the coordinated limb movements include motor pools, a topographic map, and commissural neurons[68,69,70,71,72,73,74].The activation of muscles controlling multiple joints (synergies) have been primarily described in terms of excitation[49-55]. Muscle synergies may simplify motor control in insect walking and flight [2,75,76,77,78,79].

We hypothesize that similar synergies could simplify control of the rhythmic leg movements during grooming in flies and that inhibitory circuits play a critical role. We find that inhibitory neurons target different groups of MNs, providing an alternative way to construct muscle synergies. We demonstrate that normal activity of these inhibitory neurons is essential for the rhythmic coordination of leg flexion and extension during grooming. Knocking down inhibitory receptors on MNs in flies reduces locomotion speed[80], but the specific inhibitory neurons involved remain unidentified. By analyzing limb kinematics in grooming flies and silencing specific 13A and 13B neurons, we demonstrate their critical role in spatial and temporal limb coordination. Our findings suggest inhibitory circuits play a broader role in coordinated and rhythmic limb movements.

RESULTS

We describe how inhibitory 13A and 13B neurons affect grooming. We categorize them by morphology, and map their connectivity patterns. We present evidence for muscle synergies and a role for 13A/B neurons in coordinating rhythmic limb movements. Finally, we generate a computational model to integrate and simulate our findings.

Inhibitory Interneurons in 13A and 13B Hemilineages Affect Grooming Behavior

Broad optogenetic activation of inhibitory neurons causes freezing, while activation of fewer neurons in the hemilineages 13A and 13B results in reduced grooming behavior and poor leg coordination, including static over-extension of front legs in clean or dusted flies (Figures 1D, 1F and 1F', Figure 1—Video 1). We conclude that the critical neurons are located in the ventral cord because most Split GAL4 lines only express in the VNC (Figure 1—figure supplement 1B,C, Figure 4—figure supplement 2A). For the ones that do have some brain expression, optogenetic activation in decapitated flies still produces leg extension phenotypes (Figures 1E-H, Figure 1—figure supplement 1A).

Conversely, silencing these neurons locks the front legs in flexion (Figures 1E and 1E', Figure 1—Video 1). Thus, activation or silencing of inhibitory neurons interferes with the alternation of flexion and extension required for dust removal and reduces grooming.

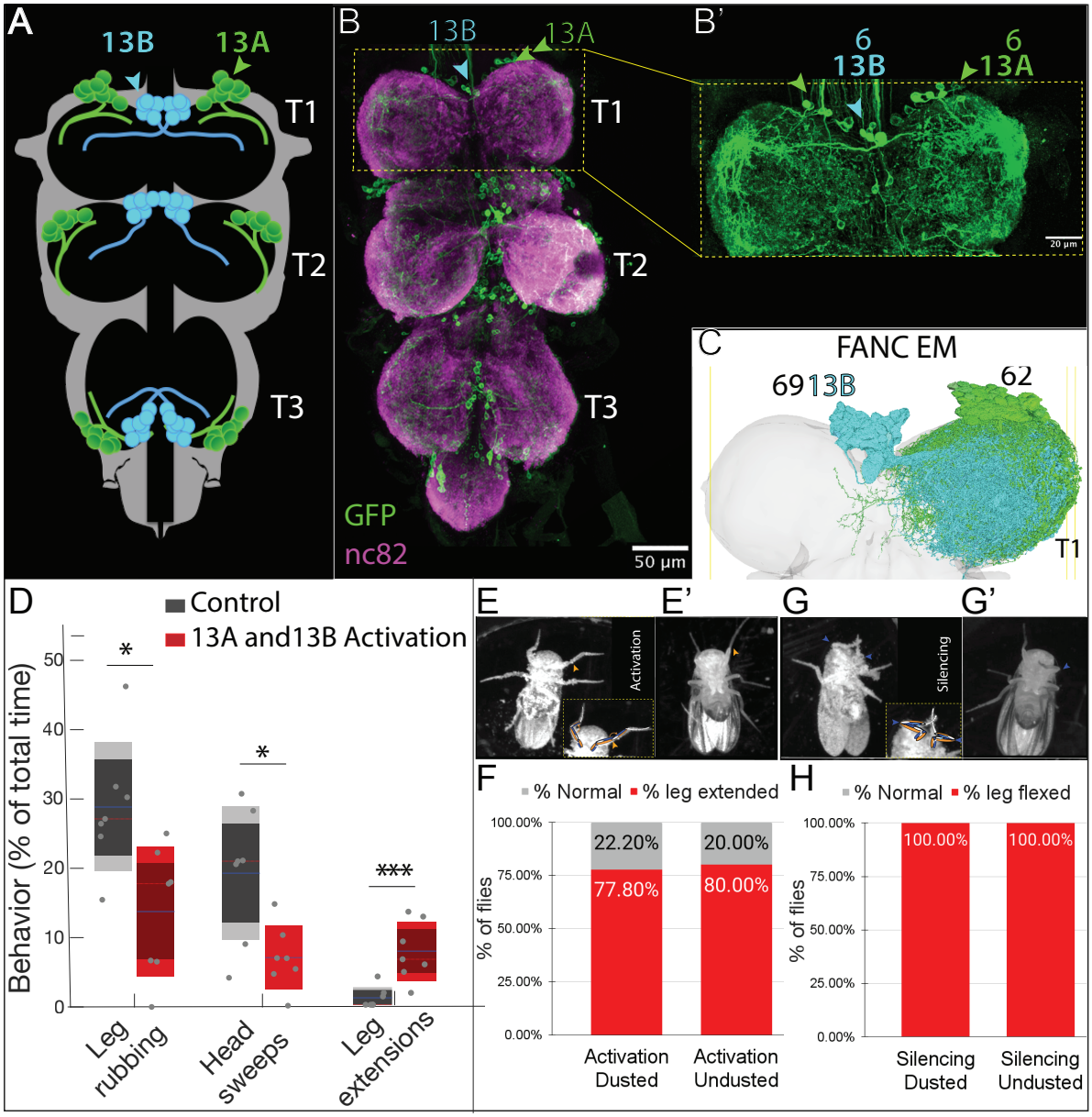

Figure 1. Anatomical Distribution and Behavioral Contributions of 13A and 13B Hemilineages

(A) Schematic showing segmental distribution of 13A (green) and 13B (cyan) neurons across pro-, meta-, and meso-thoracic segments (T1, T2, T3) of VNC.

(B) Confocal image: Six GABAergic 13A neurons (green arrowheads) and six 13B neurons (cyan arrowheads) in each VNC hemisegment, labeled with GFP (green) driven by *R35G04-GAL4-DBD, GAD-GAL4-AD*. Neuropil in magenta (nc82). Panel B' provides a zoomed-in view of T1 region.

(C) EM reconstructions: 62 13A neurons (green) and 64 13B neurons (cyan) in right T1. Ventral side up.

(D) Continuous activation of 13A and 13B neurons labeled by *R35G04-GAL4-DBD, GAD-GAL4-AD* in dusted flies reduces front leg rubbing and head sweeps, and induces unusual leg extensions. Control: *AD-DBD EMPTY SPLIT >UAS CsChrimson (gray).* Experiment: *R35G04-GAL4-DBD, GAD-GAL4-AD > UAS CsChrimson (red).* Box plots indicate the percentage of time dusted fly engaged in a given behavior over a 4-minute assay (n = 7). The solid blue line marks the mean, dark shading the 95% confidence interval, red dashed line the median, and light shading ±1 standard deviation. ****P ≤ 0.001, *P ≤ 0.05.*

(E-F) Continuous activation of 13A and 13B neuron subsets induces front leg extension in headless flies.

(E, E′) Representative video frames showing headless flies (dusted and undusted) with extended front legs (orange arrowhead) following continuous optogenetic activation of neurons labeled with *R35G04-GAL4-DBD, GAD-GAL4-AD > UAS-CsChrimson*. Dashed box in E highlights the front legs; schematic illustrates the extended posture.

(F) Quantification of leg extension phenotypes in dusted and undusted headless flies. Bar plots show the percentage of flies displaying leg extension (red) or a normal posture (gray). Percentages are calculated as the number of flies showing each posture divided by the total number of flies per condition. Dusted: n = 9; undusted: n = 5.

(G–H) Silencing 13A and 13B neuron subsets locks front legs in flexion in headless flies. (G, G′) Representative video frames showing dusted and undusted headless flies with sustained front leg flexion following silencing of neurons labeled with *R35G04-GAL4-DBD, GAD-GAL4-AD > UAS-TNTe*. Blue arrowheads indicate the flexed posture. (H) Quantification of leg flexion phenotypes in dusted and undusted headless flies. Bar plots show the percentage of flies displaying sustained flexion (red). All flies (100%) in both dusted (n = 13) and undusted (n = 9) conditions showed the phenotype. Also see Figure 1—Video 1.

Spatial Mapping and Connectivity Patterns of Premotor 13A Neurons in Leg Motor Control

The *Drosophila* nervous system develops from neuroblasts, each of which produces two hemilineages. These lineages arise from neuroblasts that divide briefly embryonically to produce primary neurons and later generate secondary neurons post-embryonically[40,41,81,82,83,84,85]. We focus on the 13A and 13B hemilineages. Using serial section electron microscopy dataset[15], we identified 62 13A neurons and 64 13B neurons in the right front leg neuromere (T1-R) of VNC. Upon entering the neuropil, 13A bundle divides into three sub-bundles, with five large neurons having extensive arbors, mostly in the ventral first sub-bundle of T1-R (Figure 2—video 1). Based on size, location, and connections, we hypothesize these represent early-born primary 13A neurons. We also identified them in the left hemisegment distributed across three sub-bundles.

Lineages contain neurons with distinct shapes and functions. We used NBLAST[86], a computational tool designed to group neurons based on morphological similarities, to categorize 13A and 13B neurons into distinct clusters (Figure 2A, Figure 2—figure supplement 3, Figure 2—video 2). Connectivity patterns were analyzed using automatic synapse detection algorithms[16]. While 13A neurons have many post-synaptic partners, their primary targets are MNs (Figure 2—figure supplement 4). Each morphological 13A cluster connects to distinct sets of MNs. Clustering by MN connections correlated with NBLAST morphological clusters, as demonstrated by a cosine similarity matrix (Figure 2 and Figure 2—figure supplement 1). While morphological and connectivity based clusters align, exceptions include cluster 9 and the 13A-3g, which have more diverse connections (Figure 2B and Figure 2—figure supplement 1 B6, H1-H9). Our initial analysis used 13A neurons in the right front leg neuromere (T1R). Comparison to a similar set on the left[21] revealed similar numbers of neurons and cluster divisions (Figure 2—figure supplement 2).

Anatomical features of 13A types suggest possible functional organization. Their dendrites occupy specific regions of VNC, suggesting common pre-synaptic inputs. Axons of 13A neurons overlap with MN dendrites (Figures 2C and 2D, Figure 2—video 3), which are spatially segregated by the leg muscles they innervate, forming a myotopic map[18,19]. Cosine similarity between morphological clusters and MN targets indicates that the spatial position of 13A neurons predicts which MN groups they connect to. Although 13A neurons respect the myotopic organization of motor neurons, many of their connections span multiple MN groups. This shows that the 13A spatial map could reflect premotor synergies (coordinated multi-joint control) rather than a strict one-to-one mapping between neurons and individual muscles.
Some 13A neurons connect to multiple MNs across various leg segments; others target only a few. We classify these as ‘generalists’ and ‘specialists’. We propose that the broadly-projecting generalists are early-born primary neurons and that the specialists that target fewer MNs are later-born secondary neurons. This is consistent with the known developmental sequence of hemilineages, where early-born primary neurons typically acquire larger arbors and integrate across broader premotor and motor targets,

whereas later-born secondary neurons often have more spatially restricted projections and specialized roles[18,19,81,82,85]. Our morphological clustering supports this idea: generalist 13As have extensive axonal arbors targeting motor neurons that control multiple leg segments, whereas specialist neurons are more narrowly tuned, connecting to a few MN targets within a segment. Thus, both their morphology and connectivity patterns align with the expectation from birth-order–dependent diversification within hemilineages. Four primary 13A neurons (13A-10f-α, -9d-γ, -10g-β, and -10e-δ) are generalists (Figure 2—figure supplement 1 I5-I8 and I9). Secondary neurons in clusters 1, 2, 4, 5, and 7 neurons are specialists, while clusters 6, 8 and 10 are generalists. Clusters 3 and 9 contain a mix. Specialist neurons tend to target MNs in a more restricted, segment-specific manner, reflecting a myotopic map, whereas generalist inhibitory neurons target specific MN groups across multiple leg segments, reflecting premotor synergies—coordinated group of muscles that work together. These overlapping patterns suggest that 13As form a spatial map organized by muscle synergies, rather than a strict one-to-one myotopic map. Together, these findings indicate that 13A neurons constitute a spatially organized premotor map, where morphology and connectivity jointly predict the recruitment of both broad, multi-joint synergies and restricted, joint-specific motor outputs.

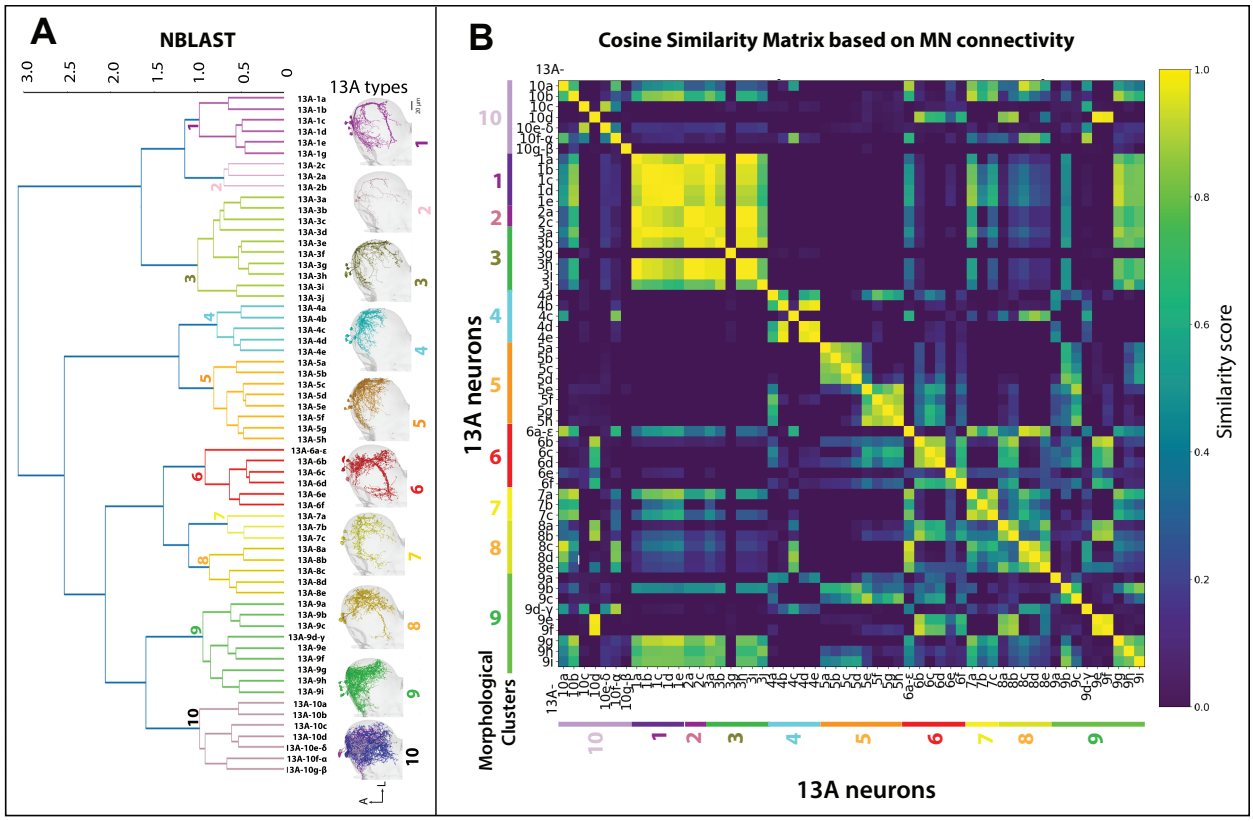

Figure 2. Spatial Map of Premotor 13A Neurons Correlates With Their Connections to Motor Neurons (MNs)

(A) Hierarchical Clustering of 13A Hemilineage. Clustering of 13A neuron types in the right T1 segment was performed using NBLAST, resulting in identification of 10 morphological groups or Clusters. EM reconstructions of distinct 13A clusters are shown. Neurons are named based on morphological clustering. For example, all neurons in the 13A-3 cluster have similar morphology, with 10 neurons labeled as 13A-3 (a-j) (olive). Images of each 13A neuron are shown in Figure 2—Figure Supplement 1. Also see Figure 2—Video 2. A= anterior, L= Lateral. Ventral side is up.

(B) **Cosine similarity graph showing pairwise similarity between 13A neurons based on their MN connectivity patterns.** 13A neurons are organized based on anatomical clusters obtained with NBLAST as described above. It depicts a correlation between anatomy of 13A neurons and their connections to MNs. For example, 13A-1a, -1b, -1c, -1d (cluster 1) connect to same set of MNs, therefore have high cosine similarity with each other (as seen across the diagonal). Graph also gives insights into groups of 13As that control similar muscles. For example, cluster 1 neurons have high cosine similarity with cluster 3 13A neurons (while, 3g neuron is an exception).

Connectivity Motifs for Coordinated Control

The adult *Drosophila* leg consists of five joints, named according to the segments they connect: bodywall/thoraco-coxal (Th-C), coxa–trochanter (C-Tr), trochanter–femur (Tr-F; fused in the adult), femur–tibia (F-Ti), tibia–tarsus (Ti-Ta). Each joint is powered by opposing flexor and extensor muscles that transmit force through tendons[15]. The proximal joints, Th-C and C-Tr, mediate leg protraction–retraction and elevation–depression, respectively[5]. The medial joint, F-Ti, acts as the principal flexion–extension hinge and is controlled by large tibia extensor motor neurons and flexor motor neurons[15,16,18,19,21]. By contrast, distal joints such as Ti-Ta and the tarsomeres contribute to fine adjustments, grasping, and substrate attachment[16].

We analyzed the connectivity of 13A/B neurons synapsing onto MNs of the medial (F-Ti) joint (Figure 3). Interconnections between 13A neuron types suggest a role in generating flexor-extensor antagonism. 13A neurons synapsing onto extensor MNs also inhibit 13A neurons targeting flexors, and vice versa (Figures 3A2, 3A3, 3B). These redundant circuits could ensure that at a given time point either extensor or flexor is active.

These 13A groups are also reciprocally connected to each other (Figures 3A4, 3A5, 3B) providing a mechanism for alternation between flexion and extension over time.

This organizational motif applies to multiple joints within a leg as reciprocal connections between generalist 13A neurons suggest a role in coordinating multi-joint movements in synergy (Figure 3C).

We did not find any correlation between the morphology of premotor 13B and motor connections, but there is a topographically restricted output based on their 13A premotor targets (Figure 2—figure supplement 1 and Figure 3—figure supplement 1B). 13B neurons connect to 13A neurons targeting either flexor or extensor MNs (Figure 3—figure supplement 1B and Figure 3—figure supplement 2). Two specific 13B neurons inhibit both extensor MNs and disinhibit flexor MNs, playing a dual role. Twenty-four 13B neurons from clusters 1 to 4 target 13A neurons.

Interconnections between 13A and 13B neurons reveal additional inhibitory motifs that could mediate movement of other joints or multiple joints synergistically. 13B neurons disinhibit MNs by inhibiting premotor 13Bs or 13As. For example, 13B-4h inhibits 13B-2i, a generalist premotor neuron targeting proximal flexor and medial extensor MNs (Figure 3—figure supplement 1 A, E, F), while preventing disinhibition of antagonistic MNs (Figures 3B and Figure 3—figure supplement 1B). Similarly, 13As could disinhibit antagonistic MNs by inhibiting premotor 13Bs. For example, primary 13A-10g-β connects to 16 13B neurons, disinhibiting proximal extensor MNs while inhibiting proximal/medial flexors (Figure 3—figure supplement 1A, D, F)

Together, inhibitory interconnections among 13A neurons, and between 13A and 13B neurons, may coordinate alternating activity in antagonistic muscle groups.

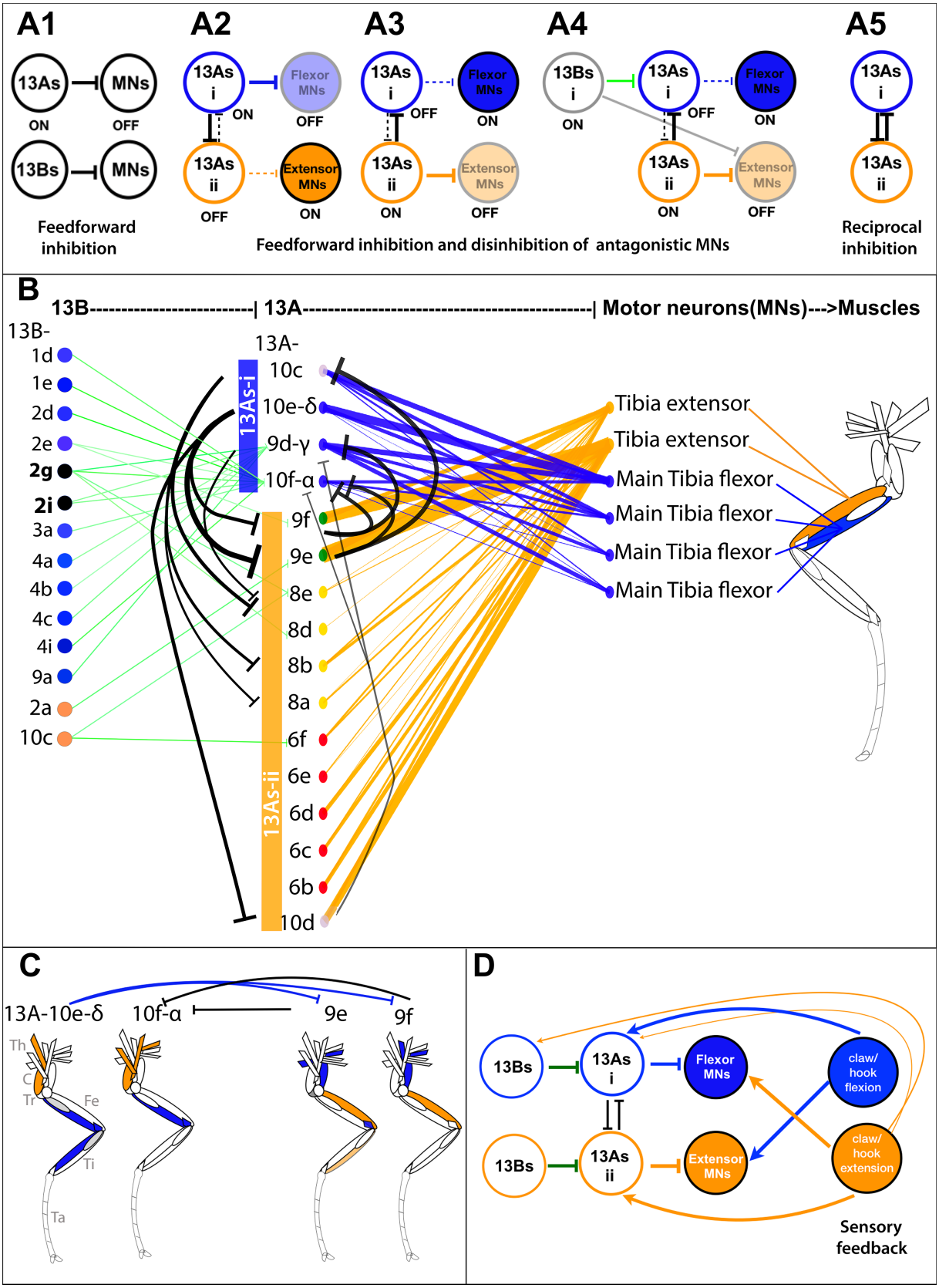
A1
13As
MNs
ON
OFF
13Bs
MNs
Feedforward inhibition
A2
13As i
Flexor MNs
ON
OFF
13As ii
Extensor MNs
OFF
ON
A3
13As i
Flexor MNs
OFF
ON
13As ii
Extensor MNs
ON
OFF
A4
13Bs i
ON
13As i
Flexor MNs
OFF
ON
13As ii
Extensor MNs
ON
OFF
Feedforward inhibition and disinhibition of antagonistic MNs
A5
13As i
13As ii
Reciprocal inhibition
B
13B----------| 13A----------| Motor neurons(MNs)--->Muscles
13B-
1d
1e
2d
2e
2g
2i
3a
4a
4b
4c
4i
9a
2a
10c
13A-
10c
10e-δ
9d-γ
10f-α
9f
9e
8e
8d
8b
8a
6f
6e
6d
6c
6b
10d
13As-i
13As-ii
Tibia extensor
Tibia extensor
Main Tibia flexor
Main Tibia flexor
Main Tibia flexor
Main Tibia flexor
C
13A-10e-δ
10f-α
9e
9f
Th
C
Tr
Fe
Ti
Ta
D
13Bs
13As i
Flexor MNs
claw/ hook flexion
13Bs
13As ii
Extensor MNs
claw/ hook extension
Sensory feedback

Figure 3. Inhibitory Circuitry for Antagonistic Muscle Control

(A) **Schematic of inhibitory circuit motifs (A1)** Feedforward inhibition by 13A/B neurons. **(A2)** Flexor inhibition and extensor disinhibition: 13As-i inhibit flexor MNs and disinhibit extensor MNs by inhibiting 13As-ii. **(A3)** Extensor inhibition and flexor disinhibition: 13As-ii inhibit extensor MNs and disinhibit flexor MNs by inhibiting 13As-i. **(A4)** 13B mediated disinhibition: 13Bs disinhibit MNs by targeting premotor 13As, while some also directly inhibit antagonistic MNs. (A5) Reciprocal inhibition among 13A groups that inhibit antagonistic MNs may induce flexor-extensor alternation.

(B) **Connectivity matrix:** Inhibitory connections regulating antagonistic MNs of the medial joint. Leg schematic shows tibia extensor (orange) and flexor (blue) muscles, innervated by respective MNs. Flexor-inhibiting 13A neurons (13As-i) in blue, and extensor inhibiting 13As (13As-ii) in orange. The thickness of edges between nodes is determined by number of synapses. Node colors were assigned based on the type of neurons, with specific colors denoting different subtypes of 13A/B neurons and MNs.

Feedforward inhibition: Primary neurons (13A-10f-α, 9d-γ, and 10e-δ) and 13A-10c (13As-i) connect to tibia flexor MNs (blue edges), making a total of 85, 219, 155, 157 synapses, respectively. Twelve secondary 13As ii inhibit tibia extensor MNs (orange edges), with strong connections from 13A-9f, -9e, and -10d totaling 188, 275, 155 synapses, respectively.

Reciprocal inhibition: Three neurons from 13As-i inhibit six from 13As ii, with 13A-10e-δ connecting to 13A-9f (19 synapses), -9e (31), and -10d (14). 13A-10c connects to 13A-8a (6), -8b (12), and -8e (5). 13A-9d-γ connects to 13A-8e (8). Conversely, three from 13As-ii inhibit two neurons from 13As i, with 13A-9f connecting to 13A-10f-α (25) and -9d-γ (6), and 13A-10d connecting to 13A-10f-α (8), -9d-γ (7), and -10e-δ (15). 13A-9e connects to 13A-10f-α (21) and -10c (47) (black edges).

Disinhibition by 13B neurons: 13B connects to 13As-i (13A-10f-α and -9d-γ) (totaling 78 and 50 synapses) (green edges), disinhibiting flexor MNs. 13B-2g and -2i also directly inhibit tibia extensor MNs.

(C) **Reciprocal inhibition for multi-joint coordination:** Primary 13As (10e-δ and 10f-α) target a combination of proximal (sternotrochanter, tergotrochanter, trochanter extensor, tergoplural promotor), medial (tibia flexor), and distal (tarsus depressor) MNs, while secondary 13As (9e and 9f) target antagonist MNs including sternal posterior rotator, pleural remotor abductor, and tibia extensor. Reciprocal connections between them indicate that generalist 13As coordinate multi-joint muscle synergies through inhibition of antagonistic motor groups. Leg schematic shows the muscles innervated by the corresponding MNs in various leg segments (Th = thorax, C = coxa, Tr = trochanter, Fe = femur, Ti = tibia, Ta = tarsus). (Data for 13A-MN connections are shown in Figure 2—figure supplement 1 I9, I6, I7, H9, H4, and H5; 13A-13A connections shown in Figure 3—figure supplement 1C).

(D) **Proprioceptive feedback:** Sensory feedback from proprioceptors onto reciprocally connected 13As could turn off corresponding MNs and activate antagonistic MNs. Flexion-sensing proprioceptors target extensor MNs and 13As-i that inhibit tibia flexor MNs. Extension-sensing proprioceptors target tibia flexor MNs and two 13As (13As-ii) that inhibit extensor MNs. Claw extension neurons also connect to 13A-δ. One 13B that disinhibits flexor MNs also receives connection from extension-sensing proprioceptors. Also see Figure 3—figure supplement 3.

Proprioceptive Feedback to 13A Neurons

We identified connections from position-sensing proprioceptors to primary 13A neurons. These could provide sensory feedback. Claw neurons detect position, while hook sense movement direction[87,88,89]. We examined reconstruction of proprioceptive neurons[20] and found multiple connections from flexion-sensing claw and hook neurons onto the main neurite of 13A-10f-α, which targets tibia flexor MNs (Figures 3D and Figure 3—figure supplement 3). Similar connections were observed onto 13A-10e-δ, -9d-γ. Recent connectome analysis showed that flexion sensing proprioceptors send direct excitatory feedback to tibia extensor MNs and indirect inhibitory feedback to flexor MNs[47]. Thus, flexion-sensing proprioceptors could activate primary 13A neurons to inhibit tibia flexor MNs, while directly activating extensor MNs. Similarly, claw extension neurons connect to two 13A neurons that target tibia extensor MNs, while directly connecting to flexor MNs. Since these two groups of 13A neurons receive proprioceptive feedback and reciprocally inhibit each other, they could drive flexion-extension alternation.

Behavioral Evidence for Muscle Synergies During Grooming

Dusted flies use their legs to perform precise grooming actions, involving repeating patterns of body sweeps and leg rubs[6,7]. Quantifying these movements using machine vision methods (DeepLabCut)[90] reveals synchronized changes in angular velocity across multiple leg joints (Figure 4A). During leg rubbing, proximal and medial joints within a given leg move predominantly in sync, as indicated by a minimal lag in their angular velocities (Figure 4A'), though they occasionally move asynchronously during head sweeps (Figure 4A"). This coordination shows the presence of muscle synergies, and generalist premotor interneuron connectivity could be how these synergies are implemented.

13A Neurons Affect Limb Coordination During Grooming

Half of the 13A population expresses a transcriptional factor, Dbx[40]. We used Split GAL4 combinations to target smaller subsets, intersecting with a GAD line and Dbx to manipulate a small subset of 13A neurons.

These 13A neurons (Figure 4B and Figure 1—figure supplement 1B) target MNs controlling multiple joints, including proximal (Th-C) (Sternotrochanter extensor, tergotrochanter, tergoplural promotor body wall muscles, and trochanter extensor MNs), medial (F-Ti) joint extensor/flexor MNs, and distal (Ti-Ta) joint tarsus extensor MN (Figure 4—figure supplement 1A1-1A3). Based on their connectivity, we hypothesized that silencing 13A neurons, and thereby removing inhibition from these MNs, would lead to exaggerated or mistimed movements at proximal and medial joints and improper positioning of the distal tarsus. Specifically, proximal joints may show excessive retraction and elevation, medial joints may display uncoordinated flexion/extension, and distal tarsus movements may become poorly targeted or overshoot, resulting in reduced inter-leg spacing and inefficient, uncoordinated grooming strokes. Conversely, activating 13As would suppress MN activity, reducing leg rotation and joint movements, limiting tibia bending and tarsus contact, and thereby impairing coordinated grooming.

To test function, we manipulated 13A neuron activity in intact, behaving animals, where motor output and sensory feedback interact continuously. This allowed us to probe their role within the intact sensorimotor system. Given their connectivity with both motor neurons and proprioceptive inputs, 13A neurons likely contribute to movement generation and its modulation by feedback. Therefore, the behavioral outcomes observed in our assays reflect their integrated role in motor control.

We measured changes in extension and flexion with joint positions, angles and inter-leg distances. Activating or silencing six 13A neurons reduced total grooming time and disrupted joint positions in dusted flies (Figure 4—figure supplement 1E'-1F'). Silencing 13A neurons reduced mean distance between F-Ti joints of the front legs (Figure 4C) and decreased the frequency of extension-flexion cycles (Figure 4F) indicating that 13A activity is required to sustain rhythmic motor output. Continuous activation of these neurons also showed a trend toward reduced frequency (though not statistically significant after correction) and increased variance suggesting that persistent activity makes the leg movements slower and more variable(Figures 4H).

To test whether these effects were specific to grooming behavior, we also examined walking bouts in these dusted flies. Silencing 13A neurons did not affect the frequency of extension–flexion cycles during walking in dusted flies (Figure 4—figure supplement 1G). However, two spatial features were altered: the distance between the tarsal tips of the front legs and the distance between the tibia–tarsus joints were both reduced, indicating subtle effects on front limb posture during walking(Figure 4—figure supplement 1G).

Silencing specific 13A neurons in dusted flies disrupted both spatial and temporal features of grooming, highlighting their necessity in producing precise grooming actions.

Furthermore, optogenetic manipulation of two different Dbx-positive 13A neurons also disrupted grooming, reducing joint position precision and mean frequency, without significantly affecting maximum angular velocity during grooming (Figure 4—figure supplement 2). Thus, 13A neurons regulate leg coordination during grooming.

13B Neurons Affect Limb Coordination During Grooming

Our experiments demonstrated that silencing or activating 13B neurons reduced grooming. Connectome data revealed that 13B neurons disinhibit groups of motor neurons. Most 13B neurons appear to act indirectly in the connectome—by contacting inhibitory neurons, potentially producing a net excitatory effect—while a subset makes direct contacts onto motor neurons. We generated a split GAL4 line that labels three 13B neurons (Figure 4B, Figure 4—figure supplement 3, and Figure 1—figure supplement 1D): two inhibit a primary 13A neuron (13A-9d-γ) which targets proximal extensor and medial flexor MNs (Figure 4—figure supplement 3C), and one is premotor, directly inhibiting both proximal and tibia extensor MNs. Together, these 13B neurons could disinhibit proximal extensor and medial flexor MNs while inhibiting medial extensor MNs.

Activating or silencing these three 13B neurons in dusted flies also reduced grooming and resulted in joint positioning defects(Figure 4D, Figure 4—figure supplement 3 D', E'). Silencing 13B neurons decreased proximal inter-leg distance(Figure 4D). Continuous activation of 13B neurons often resulted in one leg being locked in flexion while the other leg remained extended perhaps indicating contribution from unknown left right coordination circuits.

Manipulating 13B neuron activity also affects temporal aspects of grooming. Optogenetic silencing of 13B neurons in dusted flies strongly decreased mean frequencies of extension-flexion cycles of all joints (Figure 4G), while activation resulted in increased variability (Figure 4I). Both silencing or continuous activation decreased total time spent in anterior grooming, although, the bout duration of head sweeps increased upon silencing and that of leg rubs slightly reduced in dusted flies (Figure 4—figure supplement 3 F-G').

Together, 13A and 13B neurons contribute to both spatial and temporal coordination during grooming.

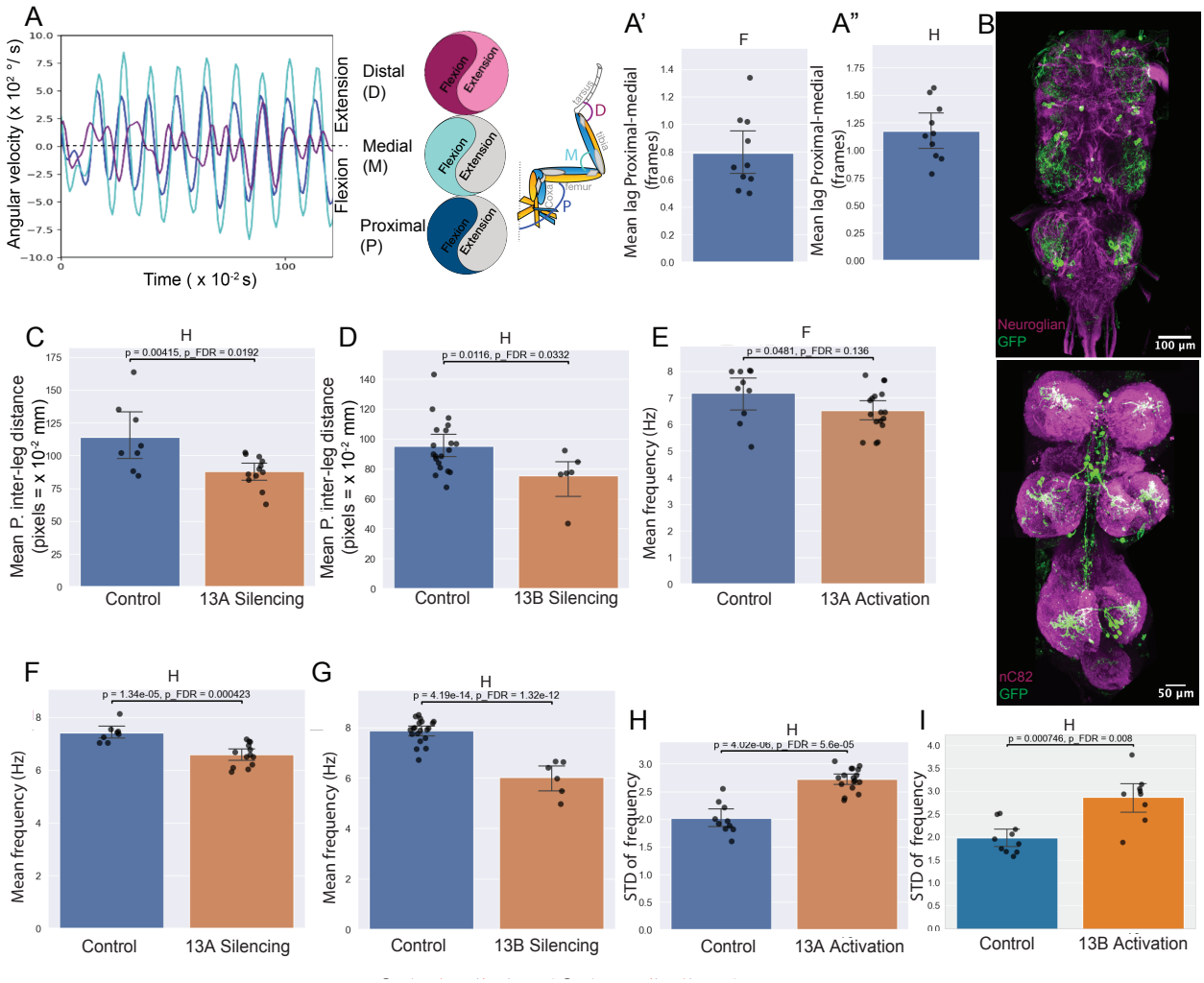

Figure 4. 13A and 13B Neurons Are Required for Leg Coordination During Grooming

(A-A") **Intra-joint coordination and muscle synergies.**

(A) Angular velocities of proximal (P, blue), and medial (M, cyan) joints predominantly move synchronously, while distal (D, purple) can move in or out of phase during leg rubbing. The schematic (right) indicates the corresponding joint angles.

(A'-A") The proximal and medial joint movements within a leg occur effectively in phase, with a mean lag of ~0.8 frames (8 ms) during leg rubbing (A′) and during head grooming sweeps (A″). Bar plots show the lag; each dot indicates one animal. Frame = 10ms.

(B) **Neuronal labeling of 13A and 13B neurons.**

Top: Confocal image of six Dbx positive 13A neurons per hemisegment labeled by GFP using *R35G04-GAL4-DBD, Dbx-GAL4-AD* in VNC. Neuroglian (magenta) labels axon bundles.

Bottom: Confocal image of three 13B neurons per hemisegment labeled by GFP using *R11B07-GAL4-DBD, GAD-GAL4-AD*. Nc82 (magenta) labels neuropil.

(C-I) **Effects of neuronal activity manipulation in dusted flies.**

Silencing and activation of 13A neurons in dusted flies using *R35G04-GAL4-DBD, Dbx-GAL4-AD with UAS Kir or UAS CsChrimson* , respectively (n=12 silencing, n=19 activation). Control: *AD-GAL4-DBD EMPTY SPLIT* with *UAS Kir or UAS CsChrimson*. For 13B neurons, *R11B07-GAL4-DBD, GAD-GAL4-AD* with *UAS GtACR1*, or *UAS CsChrimson* respectively (n=7 silencing, n=9 activation); control: *AD-GAL4-DBD EMPTY SPLIT* with *UAS GtACR1 or UAS CsChrimson*. Each panel compares control (blue) and experimental (orange) groups. Each dot represents the mean feature value for a single fly. Bars indicate the group mean, and whiskers represent the 95% confidence interval of the group mean. *P*-values (raw and false discovery rate [FDR]–corrected) are shown above each panel.

(C-D) **Proximal inter-leg distance:** Silencing of 13A (C) or 13B (D) neurons during head grooming reduces the distance between the femur-tibia joints of the left and right front legs.(E-I) **Frequency modulation:** Silencing 13A or 13B neurons reduces mean frequency of proximal joint oscillations in dusted flies.

(F, G). Activation of 13A neurons reduced frequency, although this change did not survive FDR correction. However, continuous activation of 13A and 13B neurons increased variability in frequency. (H, I). Mean of the per-animal standard deviation (STD) that reflects variability or spread of data is shown.

Activation of Inhibitory Neurons Induces Rhythmic Leg Movements

Connectome analysis revealed that inhibitory 13A and 13B neurons frequently synapse onto 13A premotor neurons. Thus, activation of these 13A or presynaptic 13B neurons should inhibit postsynaptic 13A neurons, releasing activity in MNs and promoting movement. Consistent with this connectivity, we observe that optogenetic activation of specific 13A and 13B neurons triggers grooming movements.

We also examined whether the timing of 13A activation could influence frequency of these rhythmic grooming actions. Anterior grooming actions in dusted flies are rhythmic where leg rubbing and body sweeps typically occur at a median frequency of ~7-8 Hz. One complete extension and flexion cycle, representing one sweep or leg rub, lasts ~140 ms, with 70 ms extension and 70 ms flexion phases (Figures 5B and 5B'). Connectivity analysis suggests that specific 13A neurons would be tuned to induce extension and others induce flexion, with reciprocal inhibition potentially generating rhythmicity. We optogenetically activated specific 13A neurons using 70 ms on and off

light pulses, to mimic the flexion-extension cycle, in clean flies. This indeed induced grooming (anterior and posterior) and walking (Figures 5C-5D, Figure 5—Video 1). The frequency and maximum angular velocity of proximal joint movements during these induced behaviors closely matched those observed in dust-induced grooming (Figures 5E, 5F).

To test whether the induced rhythm was locked to the stimulation period, we delivered optogenetic stimulation with equal on/off pulses of 10 ms (50 Hz), 50 ms (10 Hz), 70 ms (~7 Hz), 110 ms (~4.5 Hz), and 120 ms (~4 Hz) and compared the mean frequency of proximal joint cycles across conditions. Frequencies did not significantly differ across stimulation paradigms (Figure 5—figure supplement 1), suggesting that pulsed activation triggers the circuit's intrinsic rhythm rather than precisely pacing it.

We note that CsChrimson has relatively slow off-kinetics, which may limit the temporal precision of optogenetic control. Nevertheless, across a wide range of stimulation frequencies, optogenetic activation elicited alternating leg movements that were consistent with normal grooming behavior.

This experimental evidence shows that 13A neurons can generate rhythmic movements, reinforcing their role in coordinating grooming behavior.

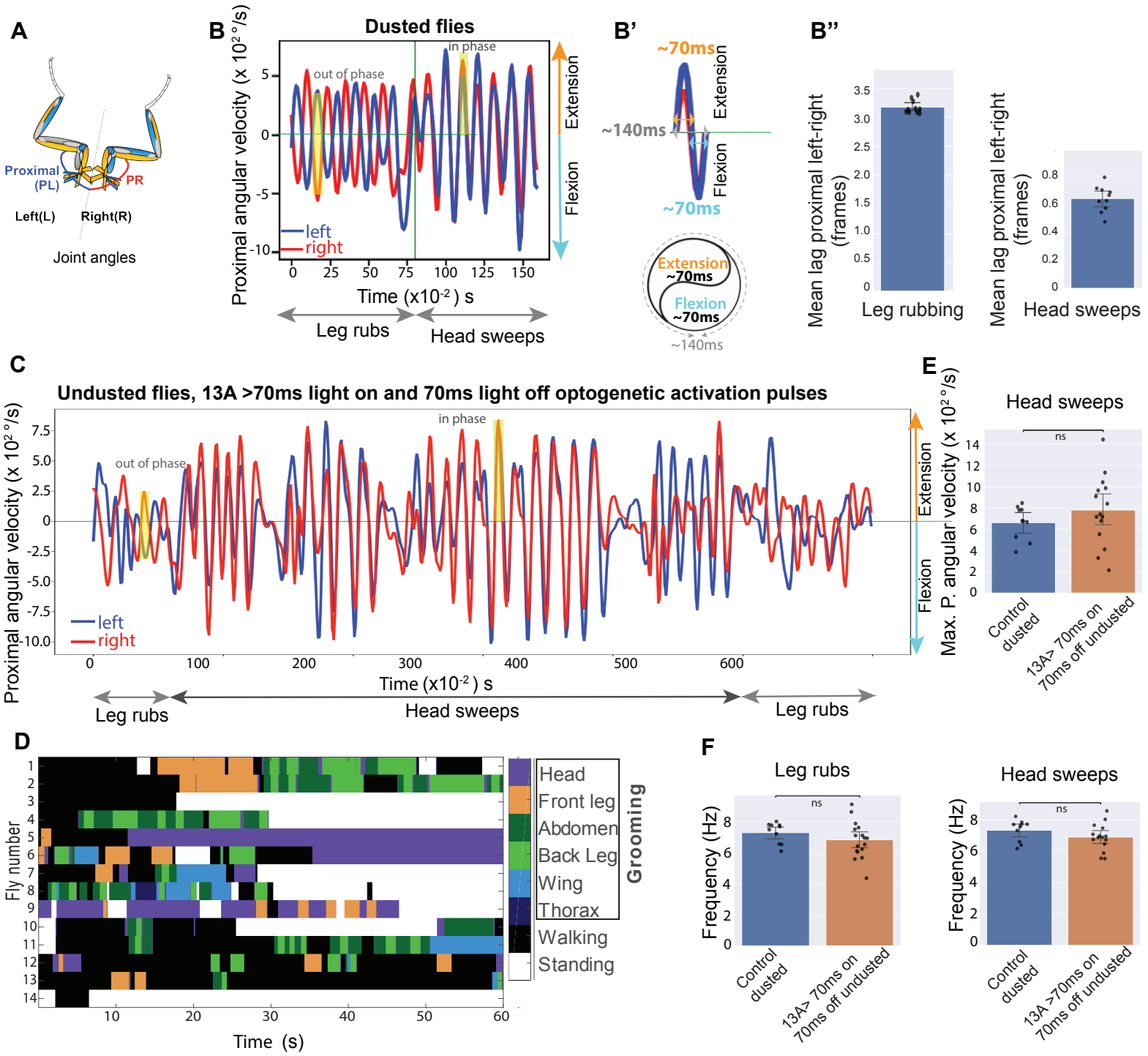

Figure 5. Pulsed Activation of 13A Neurons Triggers Rhythmic Actions in Clean Undusted Flies

(A) Schematic showing proximal joint angles of left (PL) and right (PR) legs

(B) **Left-right coordination and muscle synergies during anterior grooming.** Dusted flies perform alternating leg rubs and head sweeps. Proximal joint angular velocities are shown. PL (blue) and PR (red) joints move anti-phase during leg rubs and in-phase during head sweeps (highlighted yellow box). Positive values indicate extension, and negative indicates flexion. (B') Each flexion and extension cycle lasts ~140 ms, with each phase around 70 ms. (B'') Mean lags between proximal joints of the left and the right legs during leg rubbing and head sweeps. High lag during leg rubbing (left pannel) indicates out of phase movement and low lag during heads sweeps (right) indicates in phase movement. Bar plots show the lag; each dot indicates one animal. Frame = 10ms.

(C-F) Effect of optogenetic activation using 70ms on and 70ms off pulses in specific 13A neurons (*R35G04- DBD, Dbx-GAL4-AD >UAS CsChrimson*) in undusted flies.

(C) Angular velocity of PL and PR leg joints shows anti-phase leg rubs and sustained in-phase head sweeps, with light pulses active from time=0.

(D) Behavioral ethogram showing various grooming actions (head, front leg, abdomen, back leg, wing, thorax) and walking triggered by 70ms on and 70ms off pulsed activation of 13A neurons in undusted flies, with light pulses on from time=0.

(E) Maximum angular velocity of proximal joints during head sweeps upon pulsed 13A activation in undusted flies is comparable to that observed in dusted flies.

(F) The frequency of proximal joint movements during leg rubbing (left) and head sweeps (right) induced by 13A pulsed activation is also similar between dusted and undusted flies. *Control flies: AD-DBD EMPTY SPLIT > UAS-CsChrimson, dusted; Experimental flies: R35G04-DBD, Dbx-GAL4-AD > UAS-CsChrimson, undusted. Light pulses were delivered at 70 ms on / 70 ms off.* Each panel compares control (blue) and experimental (orange) groups. Each dot represents the mean feature value for a single fly. Bars indicate the group mean, and whiskers represent the 95% confidence interval of the group mean. *P*-values (raw and false discovery rate [FDR]–corrected) are shown above each panel.

A Computational Model of Inhibitory Circuits in Coordinating Grooming Actions

The inhibitory circuits connecting to MNs are complex and genetic reagents to target their individual components are limited, so figuring out how each component contributes to leg coordination experimentally is challenging. We developed a neural computational model based on anatomical connectivity to explore potential circuit functions. Several studies have employed (more complex) neural models to show how oscillatory behaviors, such as walking, can emerge without an explicit need for a central controller, e.g. CPG[4,91]. We modeled groups of functionally related neurons. For example, 13As that are inhibiting each other represent two groups modeled as two nodes – Figure 6A shows such a circuit for a single joint. This approach is loosely inspired by Jovanic et al., 2016[92]. Since we are not modeling individual neurons, the network does not involve spiking neurons but rather "rate based" units. The "synaptic weights" of the model

network correspond to number of synapses obtained empirically from connectome (Figure 6A).

The neural network controls movements of virtual front legs of an agent, where each leg is simplified to a 2D configuration of three segments. A pair of antagonistic “muscles” controls each of the three “joint” angles on each leg. These pairs of muscles determine the angular velocities of each “joint.” Thus each leg receives inputs from six virtual MNs. These MNs receive descending excitatory inputs, and inhibitory inputs from two 13A nodes (inhibiting the MNs of flexors and extensors). The states of the muscles (amounts of extension or flexion) are sensed by sensory neurons (SNs) that provide feedback to the 13As and to MNs. As the legs move, the most distal “joint” removes the virtual dust (Figure 6I). Legs must also spend some time in proximity to each other to remove the “dust” from themselves (This constraint forces the legs to coordinate with each other.).

The sensory input to the model circuit is a function of the distribution of “dust” remaining on the “body” - the environment—represented by the green areas in Figure 6I and Figure6-Video1). We use a small recurrent neural network (RNN) that transforms the distribution of the “dust” into excitatory inputs for the 13A network. This simple RNN, consisting of 40 units, is a “black box” used to provide the 13A circuits with excitatory sensory inputs so that the agent can respond to the changing environment. Other inputs to the "black box" include a copy of motor neuron's activation levels ("efference copy") and the amount of dust accumulated of the legs.

But the 13A circuitry can still produce rhythmic behavior even without those excitatory inputs from the “black box” (or when the inputs are set to a constant value), although the legs become less coordinated (because they are “unaware” of each other’s position at any time). Indeed, when we refine the model (with the evolutionary training) without the “black box” (using a constant input of 0.1) the behavior is still rhythmic although somewhat less sustained (Figure 7). This confirms that the rhythmic activity and behavior can emerge from the modeled pre-motor circuitry itself, without a rhythmic input.

We also added 13B nodes, as shown in Figure 6A. These nodes receive inputs from the same 'black box' as the 13As.

Figure 6B shows three types of adjacency matrices obtained from the connectome. The adjacency matrices of the model are scaled versions of these three matrices. (We assume that the ratio between the weights in each adjacency matrix, rather than the absolute numeric values in Fig 6B, reflects the connectivity.) Each adjacency matrix is scaled separately (see Methods, the fine-tuning of the synaptic weights section), preserving the ratios of synaptic weights between the same types of neurons. When we run the model with the exact values of the adjacency matrices, we do not get any behavior. So, we instead allowed the model’s parameters to deviate around their empirically obtained values. We can do this because our empirically derived weights are

not exactly represented by the weights of the modeled network. Thus, we “fine-tune” the weights, subject to constraints based on empirical values: the signs of the fine-tuned weights must remain the same as the empirical synapses (e.g. inhibitory neurons remain inhibitory), and their magnitudes have the upper and lower bounds of 20% above and below the empirical weights. No synapse can be removed from, or added to, the model by the fine-tuning process. The fine-tuning procedure was originally accomplished by genetic algorithms (GA) library PyGAD (https://pygad.readthedocs.io/en/ latest/index.html), and is currently done by our own genetic algorithm (https://github.com/PrimozRavbar/Inhibitory-circuits). The fitness function is defined as the total amount of virtual dust that the model agent removes across several episodes of grooming. The genomes contain the parameters (synaptic weights and thresholds) and hyper-parameters (see Methods). The fine-tuned weight matrices and the original ones are shown in Figures 6B-6C. Note how the ratios between synaptic weights are largely preserved.

After the fine-tuning, we analyzed the activity of the modeled 13A neural circuits, and the behavior it produced. Figure 6I shows the first, middle, and last frame of a movie. The agent succeeded in removing most of the dust (the green pixels). Figures 6D-6F shows the angles and angular velocities of the three “joints” of each front leg, and Figures 6G, 6H show the corresponding neural activity of the 13A neurons. Notice the periodic patterns in both, the motor output and the firing rates of the 13A nodes.

Next, we inquired how the model responds to perturbations analogous to the experimental activations of the 13A neurons. Figure 6J shows the dynamics of left leg joint angles in 100 renditions, when no stimulus is applied. Notice the regular periodicity of these dynamics. As we vary the length of activation pulses (Figure 6K), behavior, as reflected in angle dynamics, becomes distorted. (Legs also lose coordination and consequently less dust is removed.) These distortions also involve higher frequency of movements (see angular velocities in Figure 6K).

We also tried removing individual synaptic connections: removal of either one of the reciprocally inhibiting connections between 13As of a leg completely paralyzes it. Removing all ‘proprioceptive’ feedback from SNs to MNs does not stop the execution of the periodic movement, but it slows it down (Figure 6—figure supplement 1). Obliterating all 13A → MN synapses, not surprisingly, completely paralyzes the leg. And, when we remove just the 13A-i-MN connections (which control the flexors of the right leg) we likewise get a complete paralysis of the leg. However, removing of the 13A-ii-MN (which control the extensors of the right leg) has only modest effect on leg movements. So, we need the 13A-i neurons to inhibit the flexors (via motor neurons), but not extensors, in order to obtain rhythmic movements. Thus, our computational model confirms that rhythmic movements could be produced by inhibitory 13A circuits (even without external sensory inputs from the dust, or patterned descending input). By replicating leg movements based on real anatomical connectivity, we investigated the

potential functional roles of specific circuit components. This platform enhances our understanding of inhibitory circuits in leg coordination during grooming, providing a foundation for generating informed hypotheses in future experimental studies.

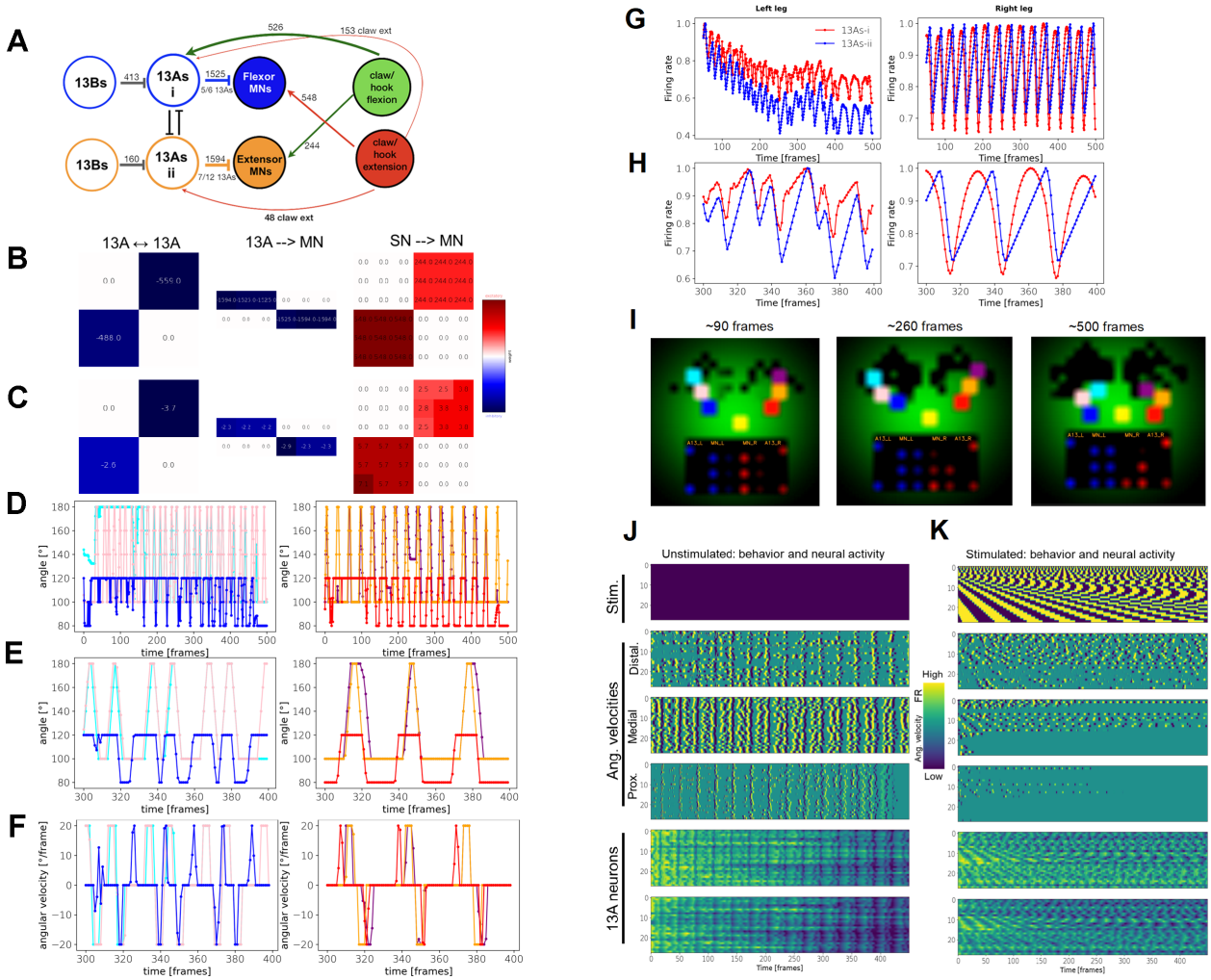

Figure 6. Modeling the 13A Circuits.

(A) Circuit diagram showing inhibitory circuits and synaptic weights based on connectome.

(B) Adjacency matrices from the empirically estimated weights, indicated in the simplified circuit diagram in (A). The 13B neurons in this model do not connect to each other, receive excitatory input from the black box, and only project to the 13As (inhibitory). Their weight matrix, with only two values, is not shown. Excitatory and inhibitory connections are shown in red and blue, respectively.

(C) Adjacency matrices of the model circuits same as in (B) but after fine-tuning. The three “joint” angles of the left leg (left) and the right leg (right) as they change over

the time of one episode (500 frames). Colors indicate “joints” as follows: distal (cyan), medial (pink), and proximal (blue) for the left leg. Right leg: distal (purple), medial (orange), and proximal (red).

(D) Same as (D) but zoomed-in to between 300-400 frames.

(E) Same as (E) but showing angular velocities [°/frame].

(F) Firing rates (activity levels) of the two 13A neurons (red and blue) over one episode (500 frames), for both legs (left, right).

(G) Same as (G) but zoomed-in to between 300-400 frames.

(H) Video frames from the beginning, middle, and end of a video of one episode. Left leg is represented by three “joints”: distal (cyan), medial (pink), and proximal (blue). Right leg: distal (purple), medial (orange), and proximal (red). The legs originate from the “base” (yellow). As legs move over the “body” (the environment – dust is represented as the green Gaussian distribution), the dust (green) is getting removed (black background). The bottom of each movie frame shows the activity of the two left 13A nodes and six left MNs (blue). The right leg nodes are shown in red, on the right side. Brightness of the nodes indicates the activity level. See Figure6-Video1.

(I) The dynamics of angular velocities of the left leg’s “joints”, and left 13A activation levels, over 100 episodes (500 frames each), when no stimulus is given (indicated by empty matrix on the top). Each row of each matrix is one episode. (The simulation started running for 50 frames before Time=0 but it starts with very high peaks which were not plotted here for better visualization.)

(J) Same as in J, but stimulation with pulses of varying durations is given. Top row of each matrix: pulse duration=2 frames; bottom (100th) row of each matrix: pulse duration=100 frames. The pulse stimulation is indicated in the top matrix.

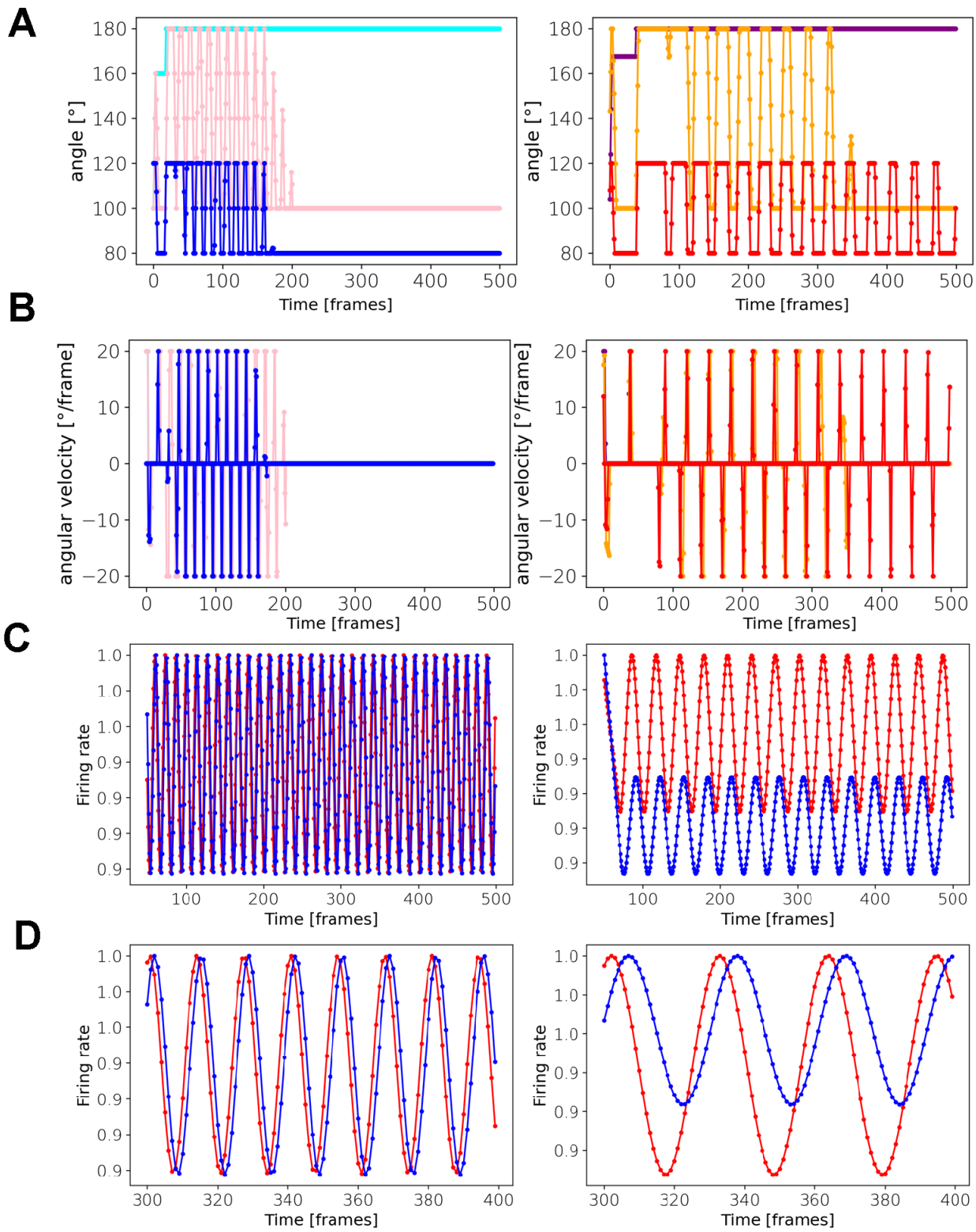

Figure 7. The Modeled 13A Circuits Can Produce Rhythmic Behavior and Activity Without Rhythmic External Input

(A) The three “joint” angles of the left leg (left) and the right leg (right) as they change over the time of one episode (500 frames). Colors indicate “joints” in the as follows: distal (cyan), medial (pink), and proximal (blue). Right leg: distal (purple), medial (orange), and proximal (red).

(B) Same as (A) but showing angular velocities [°/frame].

(C) Firing rates (activity levels) of the two 13A neurons (red and blue) over one episode (500 frames), for both legs (left, right).

(D) Same as (C) but zoomed-in to between 300–400 frames.

DISCUSSION

Inhibitory Circuit Motifs

Using VNC EM connectome data[16,20], we identified various circuit motifs formed by 13A/B inhibitory neurons that contribute to motor control.

Feed-forward inhibition: Generalist 13A neurons synapse onto multiple MNs influencing broad movements like whole leg extension, while specialist 13A neurons could refine joint-specific movements (Figure 2—figure supplement 1).

Disinhibition: 13A neurons targeting extensor MNs connect to 13As targeting flexor MNs (Figure 3), enabling flexor activation when extensors are inhibited. Generalist mediated disinhibition coordinates muscle synergies across joints, promoting leg extension or flexion. Some 13B neurons provide direct inhibition (Figure 3A), while others have an indirect effect by disinhibition of motor pools. This disinhibition motif, similar to those observed in motor systems for sequence selection[92,93,94,95,96,97,98] and flight regulation[100], may prime motor responses by holding them at the ready, to be released when inhibition is removed. Moreover, alternating inhibition and disinhibition of antagonistic motor neuron pools by premotor CPG networks has been observed previously in stick insects[25,28,79]. Disinhibitory motifs are also present in Drosophila larvae: interlinked inhibitory interneurons implement lateral and feedback disinhibition to guide sensorimotor decisions[92], and selective inhibition by premotor interneurons coordinates the sequential activation of motor neurons[99]. Our connectome analysis extends these concepts by identifying inhibitory 13A/B motifs that could implement such coordination in the adult *Drosophila* VNC to control leg movements.

Reciprocal inhibition: 13A neurons inhibiting flexors and extensors within a leg are reciprocally connected (Figure 3). This circuit resembles rIa-inhibitory neurons that are reciprocally connected circuits involved in vertebrate locomotor rhythm generation[100,101,102,103,104,105,106]. Reciprocal inhibition is also a well-established mechanism in insect motor systems: in stick insects, pilocarpine-induced rhythmic activity in deafferented nerve cords reveals strictly alternating activity between

antagonistic motor neurons[107], and intracellular recordings show cyclic hyperpolarizing inputs to flexor and extensor motor neurons in antiphase[25]. Similarly, locust thoracic ganglia exposed to pilocarpine exhibit alternating phases of antagonistic motor activity, indicating that reciprocal inhibitory motifs are a conserved solution for generating alternation[108]. Our connectomic analysis extends these classic findings by demonstrating reciprocal inhibition between inhibitory premotor 13A neurons themselves, rather than solely between antagonistic motor neurons. This additional layer of reciprocal connectivity suggests that 13As may act as a rhythm-generating kernel that shapes the timing of motor output and coordinates antagonistic activation.

Redundant inhibition: Inhibitory neurons target both MNs and their excitatory pre-synaptic partners, creating creating a parallel pathway that could modulate motor output through direct and indirect inhibition. For example, 13A-10f-α connects to both tibial flexor MNs and excitatory premotor neurons (20A/3A) that activate flexor MNs (Figure 2—figure supplement 4), preventing their activation by two parallel pathways. Similarly, the 13B-4i neuron connects to 13A neurons inhibiting flexor MNs, leading to disinhibition (Figure 3—figure supplement 2), and to excitatory neurons presynaptic to 13A neurons, thereby both removing inhibition from flexor MNs and limiting the excitatory drive onto 13A neurons.

Proprioceptive feedback onto inhibitory circuits

Position-sensing proprioceptors connect to 13As (Figures 3D and Figure 3—figure supplement 3), which inhibit flexion and disinhibit extension and vice versa, complementing reciprocal inhibition to generate alternation. Movement-sensing proprioceptors synapse onto 13A neurons, but are suppressed during walking and grooming[109]. Sherrington's 1910 proposal, supported by spinal cat studies, suggests proprioception triggers alternation—a mechanism observed in rhythmic behaviors like locust flight and mammalian respiration[110,111,112,113,114,115,116]. Connections between position sensors, 13A neurons, and antagonistic MNs suggest that proprioceptive signals may trigger alternation of leg movements during grooming.

Local and descending neurons presynaptic to reciprocally connected 13A neurons could also induce alternation. The balance between internal circuits within the central nervous system and sensory feedback contributes to pattern generation. Future studies will dissect the extent of peripheral vs. central control in generating alternation.

These motifs can explain the spatial and temporal dynamics of grooming movements. **Flexors and extensors at multiple joints must coordinate to fully extend or contract a leg.** Neurons targeting related MNs could facilitate synchronization. For example, cluster 6 or 8 13A neurons target proximal and medial joint extensor MNs, allowing leg flexion. During head sweeps, proximal and medial joints move independently—for example, the proximal joint flexes while the medial joint extends—which can be coordinated by cluster 10 13A neurons and 13A-9e, -9f.

Flexors and extensors should be mutually exclusive. A generalist connected to both proximal and medial joint MNs could facilitate leg rubbing. For example, 13A-10c synchronously inhibits proximal, medial and distal flexor MNs (Figures 3C and Figure 2—figure supplement 1I4) while targeting 13A neurons (13A-8a, -8b, and 8c) connected to extensor MNs (Figures 3F and Figure 2—figure supplement 1 G1-G3). This arrangement ensures inhibition of MNs and disinhibition of antagonistic MNs across multiple joints, preventing simultaneous coactivation.

Flexors and extensors alternate or co-contract. Reciprocal inhibition and proprioceptive feedback onto 13A neurons could facilitate alternation between extension and flexion. Reciprocal inhibition between generalist neurons of 13As-i and 13As-ii could induce alternation during head sweeps (Figure 3D). This aligns with half center model which proposes that rhythmic motor patterns arise from two mutually inhibitory neuronal populations that alternate their activity in an out-of-phase manner to drive opposing muscle groups[117,118,119]. Our behavior experiments and modeling further support this connectivity, as we indeed induced rhythmic motion through pulsed activation of specific inhibitory neurons without altering any excitatory drive. However, flexor–extensor co-contraction can also be functionally relevant, such as for modulating joint stiffness during postural stabilization or for generating large forces required for fast movements[120,121,122]. Some generalist 13A neurons could facilitate co-contraction across different leg segments, but none target antagonistic motor neurons controlling the same joint. Therefore, co-contraction within a single joint would require the simultaneous activation of multiple 13A neurons, potentially coordinated by upstream neurons that can recruit multiple 13As.

Inhibitory Innervation Imbalance Between Flexors and Extensors

We observed an imbalance in the innervation: more 13A neurons target extensors than flexors across multiple joints. While legs alternate between extension and flexion, they remain elevated during grooming. To maintain this posture, some MNs must be continuously activated while their antagonists are inactivated. Uneven distribution of inhibition could ensure that while some MNs remain active, others alternate flexion and extension in a controlled manner. Among the 13A neurons inhibiting antagonistic muscles, reciprocally connected ones could induce alternation, while others could keep legs elevated.

The asymmetry in connections, with more 13B neurons disinhibiting flexor-inhibiting 13As, suggests a mechanism for preferential flexion, supporting the flexor burst generator model, where the generator actively excites flexor MNs while inhibiting tonically active extensors[123,124].

It is important to note that our interpretations are based on connectome-derived connectivity patterns and behavioral observations from optogenetic manipulations, without direct physiological recordings from motor neurons or muscles. Studies in locust, stick insect, and cockroaches have demonstrated that fast cyclic leg movements can emerge from the interaction of rhythmic activity in a single muscle with the passive

tension of its antagonist[121,125,126,127,128]. Therefore, while our connectome analysis suggests motifs for multi-joint coordination, the exact patterns of motor neuron and muscle activity during grooming remain to be empirically confirmed.

Grooming Command Neuron Pathways to 13A Neurons

Descending neurons that command grooming movements, such as aDN[129] and DNg12[11], synapse onto 13A neurons. Although it remains unclear how constitutive activity in these descending neurons generates rhythmic grooming, the reciprocal inhibition circuits among 13As could provide a mechanism. The antennal grooming command neuron aDN synapses onto two primary 13As (γ and α; 13As-i) that connect to proximal extensor and medial flexor motor neurons, as well as four other 13As (9a, 9c, 9i, 6e) projecting to body wall extensor motor neurons. These 13As-i also form reciprocal connections with 13As-ii, potentially supporting oscillatory leg movements. aDN connects to homologous 13As on both sides, consistent with the bilateral coordination required for antennal sweeping.

The head grooming/leg rubbing command neuron DNg12 synapses onto ~50 13As, primarily those projecting to proximal motor neurons.

While structural connectivity highlights candidate pathways for rhythmic movement generation, the dense interconnections among command neurons and premotor circuits suggest that multiple motifs likely contribute to the observed behaviors. Further work is needed to determine how these pathways are dynamically recruited during natural grooming sequences.

Spatial mapping of premotor neurons in the nerve cord

The organization of 13A neurons—where morphology, position, and motor-neuron connectivity align—suggests a premotor topographic map in the fly VNC. While 13A neurons partially reflect the myotopic map of MN dendrites[18,19,130], they do not target single MNs. Instead, they form clusters that connect either to a few MNs within a segment (specialists) or to groups spanning multiple leg segments and joints (generalists). Broadly projecting generalists could recruit or inhibit coordinated sets of muscles, effectively encoding multi-joint movement patterns, whereas specialists provide more precise, segment-specific control. In other words, this map represents both the leg-muscle architecture and premotor synergies—spatially organized modules for complex actions.

Such spatial logic is consistent with other mapped systems: sensory maps in the antennal lobe preserve receptor identity[131,132,133], proprioceptors form an orderly representation of joint angles and forces in the VNC[134], or vertebrate spinal cords display dorsoventral recruitment gradients that scale locomotor output[135,136]. Together, these findings suggest that the fly VNC contains a layered spatial organization—from proprioceptive inputs to premotor and motor outputs—that could allow descending and sensory pathways to flexibly engage movement modules and synergies by addressing

specific regions of neuropil. This raises the possibility that modular movement primitives encoded in the VNC can be combined to generate diverse leg behaviors, including grooming and walking.

Computational modeling of inhibitory circuits

We employ a linear rate-based (non-spiking) neural network to represent the 13A circuitry. Natural behavior and neural activity are of course more complex. Our model explores how 13A circuit motifs could contribute to, or produce de novo, behavioral features, including rhythmic movements (which might be otherwise produced by upstream circuits), in 2D space, matching the dimensionality of our behavioral data. This abstraction is inspired by Jovanic et al, 2016[93], but we add the agent component to the neural circuitry, and apply evolutionary "fine-tuning" of parameters. Similar circuit motifs, namely reciprocal inhibitions between pre-motor neurons and the sensory feedback have been modeled before, in particular neuroWalknet, where such motifs do not require a separate CPG component to generate rhythmic behavior[4,91]. However, our neuronal model is much simpler than the neuroWalknet - it controls a 2D agent operating on an abstract environment (the dust distribution). In real animals or complex mechanical models such as NeuroMechFly[137,138], a more explicit central rhythm generation may be advantageous for the coordination across more degrees of freedom. When we perturb the model by activating 13A neurons with varying pulse lengths, we observe decreased coordination and increased movement frequency (compare angular velocities in Figure 6J with Figure 6K). Longer pulses can almost completely paralyze a leg (Fig. 6K). Here we did not attempt to simulate the exact experimental procedures. In future, the model's parameters could be fine-tuned within similarly constrained space, but with the fitness function modified: instead of parameters being optimized to remove "dust", they could be optimized by the similarity of behavioral features between the model and real flies, as has been done in whole-animal modeling[139], under various experimental conditions.

Future Directions

Our work lays groundwork for future exploration of the functional contributions of inhibitory circuits to motor control. Developing genetic tools to target specific inhibitory neurons and functional imaging during behavior would allow us to correlate temporal neuron activation with limb motion. While we focus on inhibitory control of one leg, manipulating these neurons reveals defects in left-right coordination. Investigating the circuitry involved—possibly mediated by commissural and/or descending neurons connected to these circuits—remains to be explored to elucidate the underlying circuits. Pulsed activation of 13A neurons induces grooming or walking in clean flies, while manipulating their activity in dusted flies alters grooming timing. This suggests that 13A neurons may be part of central pattern generators. While our experiments with multiple genetic lines labeling 13A/B neurons consistently implicate these cells in leg coordination, ectopic expression in some lines raises the possibility that other neurons may also contribute to these phenotypes. In addition, other excitatory and inhibitory

neural circuits, not yet identified, may also contribute to the generation of rhythmic leg movements. Future studies should identify such neurons that regulate rhythmic timing and their interactions with inhibitory circuits.

Our connectome analysis reveal that inhibitory neurons within a hemilineage form circuit motifs with complex connections to specific leg motor neurons. These neurons likely complement excitatory premotor circuits, enabling multifunctionality in behaviors such as grooming and walking. Their connectivity suggests roles in coordinating movements across multiple joints, enforcing flexor/extensor muscle antagonism, and driving extension and flexion alternation. We model and extrapolate potential functions of these complex inhibitory motifs. Normal activity of these inhibitory neurons is important for grooming; silencing or continuously activating them reduces time spent and effectiveness in dust removal, leading to forced flexion or abnormal extension, with limbs locked in extreme poses. Moreover, we show that inhibition, independent of excitatory input, plays an instructive role in generating rhythmic leg movements. Although we focus on grooming behavior, we expect these motifs to also contribute to walking, as the leg must recruit limited motor and premotor components to generate diverse movements. We conclude that inhibitory neurons are essential for controlling flexible limb movements and may play a key instructive role in timing and coordinating rhythmic behaviors.

MATERIALS AND METHODS

Contact for reagent and resource sharing

For information and inquiries regarding resources and reagents, please write to the lead contact Julie H. Simpson (**jhsimpson@ucsb.edu**).

Experimental model and subject details

Drosophila melanogaster were raised on a standard cornmeal medium at 25°C in a 12 hr light/dark cycle. For optogenetic experiments, one day old flies were transferred to food containing 0.4 mM all-trans-retinal and kept in the dark for 3 days. Genotypes of the fly lines are included in the Key Resources Table.

Identification of fly lines that target inhibitory neurons

We visually screened the VNC expression of various GAL4 lines on Flylight database[140] and compared them to the inhibitory hemilineages[41]. Next we obtained corresponding *AD, and DBD* flies from BDSC for the candidate lines and crossed them with *GAD-GAL4-AD or GAD-DBD* (Haluk Lacin) to confirm and restrict their expression in GABAergic neurons. *R35G04-GAL4-DBD, GAD-GAL4-AD* labeled six 13A and six 13B neurons per hemisegment. We also isolated six 13A neurons from this line by using *R35G04-GAL4-DBD, DBX-GAL4-AD* combination. *R11C07-GAL4-DBD and GAD-GAL4-AD* labels 4 inhibitory neurons. We intersected *R11C07 DBD* with *Dbx AD* to isolate two 13A neurons. *R11B07-GAL4-DBD, GAD-GAL4-AD* labeled 3 13B neurons.

Immunofluorescence and confocal microscopy

Flies were immobilized by anesthetizing them on ice (4°C). Central nervous system (CNS) was carefully dissected in 1X Phosphate-buffered saline (PBS). Subsequently, the wings were removed, and the flies were positioned ventral side up on a Sylgard plate. All legs were excised, and fine forceps (No. 5 Dumont from FST, Switzerland) were employed to delicately open the thorax along the midline, taking care to avoid damaging the underlying thoracic ganglia. A small incision near the first abdominal segment ensured preservation of the abdominal ganglion. Surrounding tissues were cleared from the thoracic ganglia, which were then gently extracted by grasping the neck connective. The dissected thoracic ganglia were subsequently fixed in 4% buffered paraformaldehyde for 45 minutes at 4°C.

Post-fixation, the thoracic ganglia underwent three 15-minute washes in 0.1% Triton X-100 (PBT) at room temperature on a shaker at 60 rpm, followed by a 20-minute wash in 0.1% PBT with normal goat serum (blocking solution). Primary antibodies, diluted in 0.1% PBT-NGS, were applied to the samples and incubated overnight at 4°C on a horizontal shaker. Following primary antibody incubation, the samples underwent three 15-minute washes in 0.1% PBT and one 20-minute wash in 0.1% PBT-NGS . Secondary antibodies, diluted in 0.1% PBT-NGS, were added to the samples and incubated for 2-4 hours at room temperature on a shaker at 60 rpm. Secondary antibody removal was achieved through four 15-minute washes with 0.1% PBT at room temperature. Finally, the tissues were mounted on glass slides using Vectashield mounting medium (Vector Labs).

Primary antibodies used were Chicken pAb anti-GFP (Abcam, 1:1000), Rabbit (Rb) anti-GFP (Abcam, 1:1000), mouse (ms) anti-Neuroglian (BP104) (DSHB, 1:40), ms monoclonal anti-Brp antibody (nC82) (DSHB,1:200). For MCFO labeling experiments, Rb mAb anti-HA (Cell Signaling Technologies, 1:300), Rat anti-FLAG (Novus Biologicals, 1:200), DyLight549-conjugated anti-V5 (AbD Serotec; 1:300 dilution).

Secondary antibodies from Invitrogen Molecular Probes conjugated with Alexa-488, Alexa-568 and Alexa-647 raised against chicken, ms and Rb were used in 1:400 dilution.

Zeiss LSM710 confocal microscope was used to obtain images of the CNS. Images were then processed in FIJI.

Recording and analysis of grooming in clean and dusted flies

For open field assay, we dusted the flies and obtained the recording as previously described[4]. Constant light intensity of 5.6 mW/cm² was used for continuous activation. Automated behavior analysis (ABRS) was used to quantify the amount of time flies perform individual grooming actions[141]. Additionally, manual scoring was performed[2] in flies showing uncoordinated leg movements. Quantification and statistical analysis

describing the percentage of time dusted flies spent doing grooming and uncoordinated leg movements upon 13A and B activity manipulation was performed in Matlab as previously described[9].

For limb tracking, either clean or dusted freely moving male flies were put in a studio containing 10-mm diameter quartz chamber and 100 Hz videos were recorded from below using FLIR Blackfly S camera. Custom-built LED panels (LXM2-PD01-0050, 625 nm) were utilized to deliver light activation from below, with an intensity of 1.1 mW/cm². Green led was used for silencing experiments.

Behavior analysis

Raw data, consisting of coordinates of the six annotated points on the front legs and two reference points on the body (per one frame of a video), was obtained from DeepLabCut[76]. From these coordinates we computed: 1) (fly-centric) spatial positions of the body parts, 2) the spatial velocities of the points, 3) the whole-body velocity (the translation, obtained from the reference points in absolute coordinates), 4) the euclidean distances between the leg points ("joints") and other "joints" or the reference points, and 5) the joint angles.

All behavior analysis was performed using Python, version 3.9.7.

Continuous feature extraction

The euclidean distances between various body parts (the six "joints" and the two reference points) are used as continuous features. The body velocity was computed as a euclidean distance of a point covered across a 50 frame (0.5 second) time window. Three joint angles per leg were computed from the three points on the leg and the two reference points. These angles are: posterior, medial, and distal angles. Angular velocities were computed as derivatives of the raw angles, and were lightly smoothed by a Gaussian filter (filter sigma = 2 frames). The euclidean distances were also smoothed by the same method.

The angular velocity time-series (AV) is used as the basic signal from which other continuous behavioral features are extracted, and also serves as the basis for segmentation. The main continuous features extracted from the AV are the phase and the frequencies.

The phase (between the movement of the front-legs) was computed from cross-correlation of AV signals of the two legs, using the signal.correlation_lags()function with the window for cross-correlation of five frames. We took the time-position of the maximum cross-correlation (the peak) as the lag (the phase). If the two legs are perfectly in-phase, the peak of the cross-correlation will be at time 0. The phase is a good indicator of a general type of grooming behaviors: front-leg rubbing is usually associated with a non-zero phase (a lag) wheres the head-cleaning more often than not has a zero lag (legs moving in-phase).

Frequencies are computed from the AV signal as well. We use numpy.fft.fft() function with the time window of 25 frames (0.25 seconds) and the input size of 160 frames (the length of the signal with the zero-padding) to compute the spectrum. The frequency at which the spectral power is maximal, is taken as the frequency of the signal.

Segmentation

Our analysis is focused on individual leg movements during grooming. These include contractions and extensions of the front-leg joints. For this purpose we separate the continuous features into segments corresponding to these movements.

The segmentation is performed by applying a stationary threshold to the angular velocity (AV) of the proximal joint angles. These joints determine the whole leg movements (flexions and extensions) so we consider them suitable for the purpose of segmentation. Next, for each segment we compute the averages, minima, and maxima of each continuous feature within that segment. We also compute the duration of each segment as an additional feature. These *segmented features* are used for behavioral classification and for further analysis, including comparing different groups of flies.

Classification of behavior and dimensionality reduction

We collect segments (segment features) from data-sets of groups of flies and pool them together for the purpose of classification. (e.g., experimental and control data-sets are used together.) Altogether we use 63 segment features, including averages of: euclidean distances, AVs, phases between joint pairs, frequencies of all joints, whole-body velocity, segment durations. We also include the maxima of the six AVs, and we can include combined features too (here we only use one combined feature – AV*segment duration).

For better mapping and classification of segments, we account for the temporal context of a segment: for each segment's set of features, we add the same type of features of the next two segments (in time). Thus we analyze features of triplets of segments rather than single segments.

The feature matrix X of the size f x t , where t is the total number of segments and f is the number of segment features multiplied by 3 (to account for the temporal context), is the input to the UMAP dimensionality reduction algorithm.

We use UMAP from https://pypi.org/project/umap-learn/ with the following parameters:

```
n_neighbors=350,
min_dist=0.1,
n_components=2
```

The **X** is thus projected onto two dimensions. For the UMAP construction we can remove some of the data from **X**. Namely, we can remove the data-points (segments) where angular velocity of proximal joints is below a certain value (fly is presumably not moving) or when the quality of data is too low (see quality control).

For the classification we apply the agglomerative clustering onto the 2D UMAP projection. We use AgglomerativeClustering() from sklearn.cluster (https://scikit-learn.org/stable/modules/clustering.html#hierarchical-clustering). We select the number of clusters of 12-14. Thus, we produce 12-14 class labels that can be applied to the 63 features of the segment feature matrix **X**.

Now we can compare the different behavioral classes, across the 63 features, between various groups of flies.

Comparing groups of flies

With multiple behavioral classes and features we can now compare different experimental groups of flies to assess the behavioral effects of the experimental procedures. For each *class-feature pair* we can determine whether there is a significant difference between the groups. Experimental and control groups contain data (segments) from multiple animals, so the segments from the same animal are not independent (clustered data). We therefore applied Linear Mixed Models (LMMs) to comparisons between the groups. This was accomplished by the Python method mixedlm() from statsmodels.formula.api library (https://www.statsmodels.org/stable/api.html).

The groups were compared across several features-class pairs. This calls for the multiple hypotheses adjustment. We applied the False Discovery Rate method, using the statsmodels.stats.multitest function (https://www.statsmodels.org/dev/generated/statsmodels.stats.multitest.multipletests.html). The alpha parameter was set to 0.05, and the method argument was set to fdr_bh'.

Model

The 13A circuits

The model of 13A and associated circuits was build from simple linear neuronal networks. We did not model individual neurons but rather abstracted them to nodes, interconnected by synaptic weights corresponding to the numbers of synapses obtained from the connectome analysis. Since, the 13A circuits in the right and left front leg neuropil are mirrored and there are slightly more connections on the left side (Figure 2—figure supplement 2), the synaptic weights of the same circuits on the left neuropil were used for modeling purposes.

The network is shown in Figure 6A. Below is the description of the 13A circuit model for one leg. The full model consists of two (front) legs, build the same way.

The two 13A nodes connect to each other reciprocally (inhibitory synapses). The adjacency matrix for these nodes is:

$$W_{13A \leftarrow\rightarrow 13A} = \begin{bmatrix} 0 & -559 \\ -488 & 0 \end{bmatrix}$$

The activation levels of the 13As are simply:

$$A_{13A}^{t+1} = A_{13A}^{t} + W_{13A \leftarrow\rightarrow 13A}^{T} * A_{13A}^{t} - \Theta_{13A}$$

$\mathbf{A}_{13A}$ is a vector of activation levels of the 13As, and $\boldsymbol{\theta}_{13A}$ is a vector of thresholds of 13A neurons.

The 13A nodes inhibit the six motor neurons (MNs). These connections are represented by adjacency matrix:

$$W_{13A \rightarrow MN} = \begin{bmatrix} -1594.0 & -1525.0 & -1525.0 & 0.0 & 0.0 & 0.0 \\ 0.0 & 0.0 & 0.0 & -1525.0 & -1594.0 & -1594.0 \end{bmatrix}$$

The six MNs act on the three pairs of “antagonistic muscles”, which in turn control the changes of joint angles (three per leg). Flexion and extension rates of the antagonistic muscles are directly proportional to the activation levels of the MNs.

The activation levels of the MNs are:

$$A_{MN}^{t+1} = A_{MN}^{t} + W_{13A \rightarrow MN}^{T} * A_{13A}^{t} - \Theta_{MN}$$

$\mathbf{A}_{MN}$ is a vector of activation levels of the MNs, $\mathbf{A}_{13A}$ is a vector of activation levels of 13As, and $\boldsymbol{\theta}_{MN}$ is a vector of thresholds of 13A neurons.

The inputs to the six sensory neurons (SNs) are directly proportional to the flexion and extension rates of the joint muscles. So, the activation levels of the SNs are:

$$A_{SN}^{t+1} = A_{SN}^{t} + extension/flexionrate - \Theta_{SN},$$

where $\mathbf{A}_{SN}$ is a vector of activation levels of SNs, and $\boldsymbol{\theta}_{SN}$ is a vector of thresholds of SNs.

The SNs then feed back onto both, the MNs and the 13As. The adjacency matrix representing the sensory feedback to the MNs is:

$$W_{SN\rightarrow MN} = \begin{bmatrix} 0.0 & 0.0 & 0.0 & 244.0 & 244.0 & 244.0 \\ 0.0 & 0.0 & 0.0 & 244.0 & 244.0 & 244.0 \\ 0.0 & 0.0 & 0.0 & 244.0 & 244.0 & 244.0 \\ 548.0 & 548.0 & 548.0 & 0.0 & 0.0 & 0.0 \\ 548.0 & 548.0 & 548.0 & 0.0 & 0.0 & 0.0 \\ 548.0 & 548.0 & 548.0 & 0.0 & 0.0 & 0.0 \end{bmatrix}$$

The activation levels of the MNs are then updated as follows:

$$A_{MN}^{t+1} = A_{MN}^{t} + W_{SN\rightarrow MN}^{T} * A_{SN}^{t} - \Theta_{MN}$$

where $\mathbf{A}_{MN}$ is a vector of activation levels of MNs, and $\boldsymbol{\theta}_{MN}$ is a vector of thresholds of MNs.

The adjacency matrix representing the sensory feedback to the 13As is:

$$W_{SN\rightarrow 13A} = \begin{bmatrix} 526.0 & 0.0 \\ 526.0 & 0.0 \\ 526.0 & 0.0 \\ 153.0 & 48.0 \\ 153.0 & 48.0 \\ 153.0 & 48.0 \end{bmatrix}$$

And the $\mathbf{A}_{13A}$ activation levels are updated:

$$A_{13A}^{t+1} = A_{13A}^{t} + W_{SN\rightarrow 13A}^{T} * A_{SN}^{t}$$

Activation levels are constrained as follows:

- max($\mathbf{A}_{13A}$) = 2500
- max($\mathbf{A}_{MN}$;$\mathbf{A}_{SN}$) = 200

Minimal activation levels for all neurons are set at zero (so, no negative rates).

Two 13B nodes were added to inhibit the two 13A nodes. The initial weights of the 13B --> 13A were -413 and -160.

<u>The excitatory network</u>

The model network also needs an excitatory input. Because we do not know the upstream excitatory connections from the connectome we created a “black box” network that takes the simulated dust distribution as the input, and it outputs excitatory signal to the 13A, 13B, and MNs. Other inputs include: the “proprioceptive” inputs (“efference copy” from motor neurons), and the amount of dust accumulated on both legs. The “black box” excitatory network consists of a recurrent neural network (RNN) as the hidden layer, with linear synapses and initially random wights.

The hidden RNN layer has 40 nodes. The input layer is the dust grid and the pixel values are its the inputs. The output layer has 21 nodes connecting to the two 13B nodes, the two 12A nodes, and the 6 MN nodes, *per one leg* (so 10 outputs per leg). The same excitatory network also feeds to the other leg’s 13A network, in the same manner. The remaining output node does not project anywhere (it is placed there for future model development where it could output the amplitude of exploratory noise injected into the 13A network).

The agent and the environment

Our model is composed of neuronal circuits embedded in a simple agent that acts on its environment. The agent has two 2D legs, corresponding to the two front legs of a fly, each of which is made of three points (“joints”): proximal, medial, and distal. The distal point (the one farthest from the “body”) can remove the “dust” from the environment. The movement of the “joints” (per leg) is controlled by three pairs of “antagonistic muscles” affecting the three angles formed by the “joints.” Figure 6I shows a frame of a movie where the legs are represented by the three points each.

The environment is composed of a Gaussian distribution of “dust” around the agent (green pixels in Figure 6I). The means of the Gaussian are at the center of the 32 by 32 pixel grid (also the position of the “root” of the front legs), so x=0; y=0. The variance = 5 pixels, in both directions. The maximal amount of dust (at the peak of the Gaussian) is 1.0 (0.99).

The agent can remove the “dust” when the distal “joint” sweeps over the environment with the minimum velocity of 1 pixel/frame. (So, if the “joint” just stays at a given position, the dust is not getting removed. It has to move over it.)

As the grooming behavior is being performed, the “dust” accumulates on the legs, reducing their ability to continue removing it from the grid (the “body”). The “leg cleaning” - removal of the accumulated dust occurs when the two legs are in proximity to each other (Euclidean distance < 5 pixels). The “leg cleaning” rate of dust removal from legs is the same as the body dust removal rate: 0.5/frame.

The three angles (per leg) are constrained. Distal and medial angles: 100° - 180°; proximal angle: 80° -120°.

The fine-tuning of the synaptic weights

When we run the model with the default synaptic weights (see previous sections) nothing happens, i.e. the activation levels either saturate (reach the ceiling values shown above)fall to zero, or reach a steady value. The legs of the agent may move once or twice and then the model "freezes." One way of getting around this problem would be to add a "CPG component" to the model, to drive the periodic excitatory inputs, thereby creating a baseline periodic activity and movements. We could then study the effects of the 13A circuitry on these movements. However, we wanted to see if the model network could generate periodic movements all by itself.

The empirical weights used in the model are approximate and we do not know the exact ratios between individual modeled weights (the assumption is that the number of biological synapses corresponds to the weights). So, we allow the modeled weights to vary (in value, but not in sign) and yet preserve the approximate ratios obtained from the empirical data. In other words, we are exploring a space of possible models that adhere to approximately the weight ratios obtained empirically. Specifically, the weights are allowed to vary +/- 20% and cannot change the sign – i.e. inhibitory neurons must remain inhibitory. (In future work we may decrease this space of exploration to adhere even more closely to the empirical estimates. Conversely, we may increase the exploration space and observe all solutions to see how close our empirical estimates are to the global optimum.)

We thus constrain the model to the connectome as follows:

The connectome matrix reference $\mathbf{W}_{\mathbf{ref}}$ contains the empirical weights for a given neuron type (e.g. $\mathbf{W}_{\mathbf{13A} \longleftrightarrow \mathbf{13A}}$) and $\mathbf{W}_{\mathbf{mod}}$ contains the weights from the evolving model (see below). First we eliminate non-zero weights from the model ($\mathbf{W}_{\mathbf{mod}}$) that should be zero in the reference matrix $\mathbf{W}_{\mathbf{ref}}$:

$$M_{ij} = \begin{cases} 1 & \text{if } \mathbf{W}_{\text{ref},ij} \neq 0 \\ 0 & \text{if } \mathbf{W}_{\text{ref},ij} = 0 \end{cases}$$

$$\mathbf{W}_{\text{masked}} = M \odot \mathbf{W}_{\text{raw}}$$

Because the absolute numbers in the empirical matrices ($\mathbf{W}_{\mathbf{ref}}$) are meaningless for the modeling we can rescale them -assuming that same the ratios of the synaptic weights between the same types of neurons are preserved. So, each adjacency matrix connecting the same type of neurons is scaled separately. For example, $\mathbf{W}_{\mathbf{13A} \rightarrow \mathbf{MN}}$ is

specifying the connections between 13As and MNs, and is thus scaled separately from $\mathbf{W}_{13A \longleftrightarrow 13A}$ which specifies connections between 13As. Each $\mathbf{W}_{ref}$ is scaled as shown:

$$a_{\text{raw}} = \max_{i,j} \left|\mathbf{W}_{\text{masked},ij}\right|, \quad a_{\text{ref}} = \max_{i,j} \left|\mathbf{W}_{\text{ref},ij} \cdot M_{ij}\right|$$

$$\mathbf{W}_{\text{ref}}^{\text{scaled}} = \frac{a_{\text{raw}}}{a_{\text{ref}}} \mathbf{W}_{\text{ref}}$$

We then compute the tolerance bounds, where tolerance τ = 0.2:

$$\mathbf{W}_{\min} = (1-\tau)\,\mathbf{W}_{\text{ref}}^{\text{scaled}}, \quad \mathbf{W}_{\max} = (1+\tau)\,\mathbf{W}_{\text{ref}}^{\text{scaled}}$$

Finally we enforce sign constraints and clip the model matrix $\mathbf{W}_{mod}$:

$$\mathbf{W}_{\text{signed},ij} = \left|\mathbf{W}_{\text{masked},ij}\right| \operatorname{sgn}(\mathbf{W}_{\text{ref},ij})$$

$$\mathbf{W}_{\text{mod},ij} = \begin{cases} \min\Big(\max(\mathbf{W}_{\text{signed},ij}, \mathbf{W}_{\min,ij}), \mathbf{W}_{\max,ij}\Big) & \text{if } M_{ij} = 1 \\ 0 & \text{if } M_{ij} = 0 \end{cases}$$

To explore the space around our empirically estimated weights, we employed a genetic algorithm (GA) that we wrote (see the model code at https://github.com/PrimozRavbar/Inhibitory-circuits) Briefly, we evolved a population of 250-500 genomes containing the model parameters (weight matrices, thresholds) and hyper-parameters (max firing rates). The mutation rate was set to 0.1. The genomes were competing in cohorts of 6. At each epoch (each genome – agent – in the cohort played 2 “games”) fitness rates were assigned and the strongest genomes were allowed to reproduce accordingly. *There was no cross-over*. Importantly, for every new generation the mutated genomes were adjusted to fit the empirical weights within the tolerance limit of 0.2 (clipped, as described above). This way the evolutionary exploration remained bounded throughout the process.

Connectome analysis

Neuronal reconstruction, lineage identification and detection of neuronal partners

We used serial-section transmission electron microscopy (TEM) dataset of female adult *Drosophila* (FANC)[20] to reconstruct 13A and 13B hemilineages in the VNC. These neurons were identified in the EM volume based on their cell body clusters, arborization

pattern and nerve bundle entry positions into the ventral neuropil[40,41,81] and comparison with light-level images and axonal tracts labeled with anti-Neuroglian.

13A neurons cluster together and enter the VNC neuropil anteriorly through the ventrolateral position[40,41,81,142]. 13B neurons have contralateral cell bodies and ipsilateral projections, with their axons entering the neuropil through the extreme ventral bundle[40,41,81]. Using confocal microscopy images of 13A and 13B neurons marked with GFP and axonal tracts labeled with anti-Neuroglian for reference comparison, we located these neurons in the EM volume. We manually traced the main neural skeletons and later proof-read automatic segmentations. Then neuronal IDs and cell body coordinates of each 13A and 13B neurons is shown in Table S1.

Manual reconstructions of some of the 13A and 13B neurons were initially performed in CATMAID[143]. Traced skeletons were then imported from CATMAID to Neuroglancer[144]. We identified other 13A neurons and 13B neurons in the corresponding hemilineage bundles and proofread errors in the automated neuronal reconstructions[16]. We fully proofread 62 13A neurons (Table S1), 64 13B neurons in the right prothoracic segment (T1) of VNC, and 25/64 13B neurons in the left T1. We used the automated synapse detection to identify the downstream and upstream connections[16]. We used various FANC packages[16] generously available to the community to generate upstream and downstream partner summary of all the 13A and 13B neurons in R studio (https://rdrr.io/github/flyconnectome/fanc/man/fanc_partner_summary.html).

Connectivity matrix

To plot connectivity matrices between groups of neurons, we utilized Python libraries including pandas, networkx, and matplotlib. We created a directed graph using networkx to represent the connections, where presynaptic and postsynaptic neurons were added as nodes. The thickness and color of edges between nodes were determined by the strength of the connections, and the type of presynaptic or postsynaptic neurons, respectively. Node colors were assigned based on the type of neurons, with specific colors denoting different subtypes of 13A/B neurons and MNs. Finally, we generated the visualization using matplotlib. 13B to 13A connections were manually added in Figure 3B. Leg schematic and MN to muscle connections were also manually added in Adobe Illustrator.

Cosine similarity matrix

We computed the cosine similarity matrix of 13A neurons based on their downstream motor connections in Python using the cosine_similarity from sklearn.metrics.pairwise for computing cosine similarities. A pivot table was created from the DataFrame, with neurons as rows (index) and their post-synaptic targets (post_id) as columns. The values in this table represented the weights of the connections. Duplicates were aggregated using the sum function, and missing values were filled with zeros. The cosine similarity between each pair of neurons was calculated using the

cosine_similarity function. Cosine similarity is a measure that calculates the cosine of the angle between two vectors. In this context, each neuron is represented as a vector of its connectivity weights to downstream MNs. The cosine similarity value ranges from -1 to 1, where: 1 indicates that the vectors are identical. 0 indicates that the vectors are orthogonal (no similarity). -1 indicates that the vectors are diametrically opposed. This calculation resulted in a similarity matrix, where each entry (i, j) represents the cosine similarity between the connectivity profiles of neuron i and neuron j. This calculation resulted in a similarity matrix, where each entry (i, j) represents the cosine similarity between the connectivity profiles of neuron i and neuron j. The resulting cosine similarity matrix was visualized using matplotlib. The matrix was displayed as a heatmap with a color gradient indicating the degree of similarity.

Classification of 13A and 13B neurons based on morphology

We used NBLAST[16,86], a computational method to measure pairwise similarity between neurons based on their position and geometry to identify various subclasses within the hemilineages. We performed hierarchical clustering on pairwise NBLAST similarity scores computed using navis.nblast_allbyall(). The resulting similarity matrix was symmetrized by averaging it with its transpose, and converted into a distance matrix using the transformation:
distance=(1−similarity)\text{distance} = (1 - \text{similarity})distance=(1−similarity)
This ensures that a perfect NBLAST match (similarity = 1) corresponds to a distance of 0.
Clustering was performed using Ward's linkage method (method='ward' in scipy.cluster.hierarchy.linkage), which minimizes the total within-cluster variance and is well-suited for identifying compact, morphologically coherent clusters. We did not predefine the number of clusters. Instead, clusters were visualized using a dendrogram, where branch coloring is based on the default behavior of scipy.cluster.hierarchy.dendrogram(). By default, this function applies a visual color threshold at 70% of the maximum linkage distance to highlight groups of similar elements. In our dataset, this corresponded to a linkage distance of approximately 1–1.5, which visually separated morphologically distinct neuron types (Figures 2A and Figure 2—figure supplement 3A). This threshold was used only as a visual aid and not as a hard cutoff for quantitative grouping.This classification was based on similarity scores and included left-right comparisons.

RESOURCES TABLE

REAGENT or RESOURCE	SOURCE	IDENTIFIER

Antibodies		
Chicken polyclonal anti-GFP	Abcam	RRID: AB_300798
Rabbit (Rb) polyclonal anti- GFP	Invitrogen	Cat #A11122; RRID: AB_221569
Mouse (ms) monoclonal anti-Bruchpilot	DSHB	RRID: AB_2314866
ms anti-Neuroglian (BP104)	DSHB	RRID: AB_528402
Mouse polyclonal anti-V5:DyLight 550	AbD Serotec	RRID: AB_2687576
Rabbit polyclonal anti-HA	Cell Signaling Technologies	RRID: AB_1549585
Rat monoclonal anti-FLAG	Novus Bio	RRID: AB_1625982
Goat anti-Chicken Alexa Fluor 488	Invitrogen	RRID:AB_142924
Goat anti-rabbit Alexa Fluor 488	Invitrogen	RRID. AB_143165
Goat anti-mouse Alexa Fluor 568	Invitrogen	RRID: AB_2534072

Goat anti-mouse Alexa Fluor 633	Invitrogen	RRID:AB_2535719
Goat anti-rabbit Alexa Fluor 568	Invitrogen	RRID: AB_143157
Goat anti-rat Alexa Fluor 488	Invitrogen	RRID: AB_2534074
Donkey anti-rat Alexa 647	Jackson ImmunoResearch	RRID: AB_2340694
Chemicals, Peptides, and Recombinant Proteins		
Insect-a-slip	Bio Quip Products	Cat#2871A
Reactive Yellow 86	Organic Dyestuffs Corporation	CAS 61951-86-8
Experimental Models: Organisms/Strains		
R35G04-GAL4-DBD	Bloomington Stock Center (BDSC)	RRID: BDSC_70351
GAD-GAL4-AD	Deng et al., 2019	
GAD-GAL4-DBD	Gift from Haluk Lacin and James Truman	

Dbx-GAL4-AD	Gift from Haluk Lacin and James Truman	
Dbx-GAL4-DBD	Gift from Haluk Lacin and James Truman	
R11C07 AD	BDSC	RRID: BDSC_70533
w[1118]; P{y[+t7.7] w[+mC]=20XUAS-IVS-CsChrimson.mVenus} attP40	BDSC	RRID: BDSC_55135
P{JFRC7-20XUAS-IVS-mCD8::GFP} attp40	BDSC	RRID: BDSC_32194
UAS-GTACR1	Gift from Adam Claridge-Chang	
w[*]; P{y[+t7.7] w[+mC]=UAS-GtACR1.d.EYFP}attP2	BDSC	RRID: BDSC_92983

w[1118] P{y[+t7.7] w[+mC]=R57C10-FLPL} su(Hw)attP8; PBac{y[+mDint2] w[+mC]=10xUAS(FRT.stop)myr::smGdP-HA} VK00005 P{y[+t7.7] w[+mC]=10xUAS(FRT.stop)myr::smGdP-V5-THS-10xUAS(FRT.stop)myr::smGdP-FLAG} su(Hw)attP1(MCFO3)	BDSC	RRID: BDSC_64087
10XUAS-IVS-eGFP-Kir2.1	von Reyn et al., 2014	
Control-GAL4-AD-GAL4-DBD EMPTY SPLIT: BPp65ADZp(attp40); BPZpGDBD(attp2)	BDSC	RRID: BDSC_79603
Software and Algorithms		
DeepLabCut	Mathis et al., 2018	RRID:SCR_021391
Python		RRID:SCR_008394
MATLAB	MathWorks	RRID: SCR_001622
FIJI	Schindelin et al., 2012	RRID:SCR_002285
Adobe illustrator		RRID:SCR_010279

Adobe Photoshop		RRID:SCR_014199
Braincircuits		https://braincircuits.io/app?p=fruitfly_fanc_public
Neuroglancer	Maitin-Shepard et al., 2021	RRID:SCR_015631
fancr	FANC packages	https://github.com/flyconnectome/fancr
neuPrint	Plaza et al., 2022	https://neuprint.janelia.org/
CATMAID	Saalfeld et al., 2009	RRID:SCR_006278
RStudio		RRID:SCR_000432

ACKNOWLEDGEMENTS

We thank UCSB undergraduate members, especially Ethan Zhang, Yarah Meijer, Daniel Perry, Kaya Minami, and Allene Dang for experimental assistance and proofreading neurons. Sara Abraham, E.Z., Y.M., and K.M. contributed to manual behavioral labeling. Gabe Bello, Katelyn Ross, Kelly McDonald, Kai Thomas, Jada Moore, Yash Shah, Jinyi Dong, Mark Lu, Charliene Lien, Sofia Easton, William Jaber, Paige Gambetta, Maya Teitz, Dhruvi Dalwadi, Abdallah Samarah, Jonathan Carranza, Chandni Patel, Hana Nguyen, Inzar Khan, Garima Sehgal, Sydney Mauch, Yida Huang, Liz Kaslewicz, Nina Shenoy, Joseph Perliss, and Lindsay Easter proofread 13A/B neurons and their partners in the EM dataset. Y.M., K.R., M.T., K.M., G.B., Y.S., J.M., L.E. led the EM team, with training provided by Li Guo, David McNeill, Ladann Kiassat, G.B., E.Z., and Y.M.

We thank Wei-Chung Allen Lee, John Tuthill, and Jasper Phelps for access to the FANC connectome, the FANC community for generously sharing resources, and the Janelia and Cambridge groups for the MANC data.

We are grateful to Akinao Nose and Shingo Yoshikawa for manuscript feedback. For fly strains, we thank James Truman, Haluk Lacin, Gerald Rubin, Benjamin White, Adam Claridge-Chang, and the Bloomington Drosophila Stock Center (NIH grant P40OD018537). This work was supported by NSF Career Award IOS-1943276 and NIH grant RF1NS132900.

AUTHOR CONTRIBUTIONS

D.S.S. **:** Conceptualization, Investigation, Methodology, Formal analysis, Writing – original draft, review and editing. P.R. **:** Modeling, Methodology, Software, Formal analysis. J.H.S. **:** Conceptualization, Funding acquisition, Supervision, Writing – review and editing.

DECLARATION OF INTERESTS

The authors declare no competing interests.

REFERENCES

[1] Cruse H. What mechanisms coordinate leg movement in walking arthropods? Trends Neurosci. 1990 Jan;13(1):15-21. doi: 10.1016/0166-2236(90)90057-h.

[2] Berkowitz A, Laurent G. Central generation of grooming motor patterns and interlimb coordination in locusts. J Neurosci. 1996 Dec 15;16(24):8079-91. doi: 10.1523/JNEUROSCI.16-24-08079.1996.

[3] Dürr V, Ebeling W. The behavioural transition from straight to curve walking: kinetics of leg movement parameters and the initiation of turning. J Exp Biol. 2005 Jun;208(Pt 12):2237-52. doi: 10.1242/jeb.01637. PMID: 15939767.

[4] Schilling M, Cruse H. Decentralized control of insect walking: A simple neural network explains a wide range of behavioral and neurophysiological results. PLoS Comput Biol. 2020 Apr 27;16(4):e1007804. doi: 10.1371/journal.pcbi.1007804.

[5] Büschges A, Ache JM. Motor control on the move: from insights in insects to general mechanisms. Physiol Rev. 2025 Jul 1;105(3):975-1031. doi: 10.1152/physrev.00009.2024.

[6] Ravbar, P., Zhang, N., & Simpson, J. H. (2021). Behavioral evidence for nested central pattern generator control of *Drosophila* grooming. *eLife, 10*, e71508. https://doi.org/10.7554/eLife.71508

[7] Seeds, A. M., Ravbar, P., Chung, P., Hampel, S., Midgley, F. M., Jr, Mensh, B. D., & Simpson, J. H. (2014). A suppression hierarchy among competing motor programs drives sequential grooming in Drosophila. *eLife, 3*, e02951. https://doi.org/10.7554/eLife.02951

[8] Hampel, S., McKellar, C. E., Simpson, J. H., & Seeds, A. M. (2017). Simultaneous activation of parallel sensory pathways promotes a grooming sequence in Drosophila. *eLife, 6,* e28804. https://doi.org/10.7554/eLife.28804

[9] Zhang, N., Guo, L., & Simpson, J. H. (2020). Spatial Comparisons of Mechanosensory Information Govern the Grooming Sequence in Drosophila. *Current biology : CB*, *30*(18), 3697–3698. 10.1016/j.cub.2020.01.045

[10] Zhang, N., & Simpson, J. H. (2022). A pair of commissural command neurons induces Drosophila wing grooming. *iScience, 25*(2), 103792. https://doi.org/10.1016/j.isci.2022.103792

[11] Guo, L., Zhang, N., & Simpson, J. H. (2022). Descending neurons coordinate anterior grooming behavior in Drosophila. *Current biology : CB, 32*(4), 823–833.e4. https://doi.org/10.1016/j.cub.2021.12.055

[12] Eichler, K., Hampel, S., Alejandro-García, A., Calle-Schuler, S. A., Santana-Cruz, A., Kmecova, L., Blagburn, J. M., Hoopfer, E. D., & Seeds, A. M. (2024). Somatotopic organization among parallel sensory pathways that promote a grooming sequence in Drosophila. *eLife, 12,* RP87602. https://doi.org/10.7554/eLife.87602

[13] Yoshikawa, S., Tang, P., & Simpson, J. H. (2024). Mechanosensory and command contributions to the Drosophila grooming sequence. *Current biology : CB, 34*(10), 2066–2076.e3. https://doi.org/10.1016/j.cub.2024.04.003

[14] Miller, A. (1950). The internal anatomy and histology of the imago of Drosophila melanogaster. In Biology of Drosophila (ed. M. Demerec), pp.420-531. New York, NY: John Wiley &Sons.

[15] Soler, C., Daczewska, M., Da Ponte, J. P., Dastugue, B., & Jagla, K. (2004). Coordinated development of muscles and tendons of the Drosophila leg. *Development, 131*(24), 6041–6051. https://doi.org/10.1242/dev.01527

[16] Azevedo, A., Lesser, E., Mark, B., Phelps, J., Elabbady, L., Kuroda, S., Sustar, A., Moussa, A., Kandelwal, A., Dallmann, C.J., et al. (2024). Connectomic reconstruction of a female Drosophila ventral nerve cord. *Nature*, doi: https://doi.org/10.1038/s41586-024-07389-x

[17] Azevedo, A.W., Dickinson, E.S., Gurung, P., Venkatasubramanian, L., Mann, R.S., Tuthill, J.C., 2020. A size principle for recruitment of Drosophila leg motor neurons. *eLife 9*, e56754. https://doi.org/10.7554/eLife.56754

[18] Baek, M., & Mann, R. S. (2009). Lineage and birth date specify motor neuron targeting and dendritic architecture in adult Drosophila. *The Journal of neuroscience 29*(21), 6904–6916. https://doi.org/10.1523/JNEUROSCI.1585-09.2009

[19] Brierley, D. J., Rathore, K., VijayRaghavan, K., & Williams, D. W. (2012). Developmental origins and architecture of Drosophila leg motoneurons. *The Journal of comparative neurology*, *520*(8), 1629–1649. https://doi.org/10.1002/cne.23003

[20] Phelps, J.S., Hildebrand, D.G.C., Graham, B.J., Kuan, A.T., Thomas, L.A., Nguyen, T.M., Buhmann, J., Azevedo, A.W., Sustar, A., Agrawal, S., et al. (2021). Reconstruction of motor control circuits in adult Drosophila using automated transmission electron microscopy. *Cell*, *184*(3), 759–774.e18. https://doi.org/10.1016/j.cell.2020.12.013

[21] Lesser, E., Azevedo, A. W., Phelps, J. S., Elabbady, L., Cook, A., Syed, D. S., Mark, B., Kuroda, S., Sustar, A., Moussa, A., et al. (2024). Synaptic architecture of leg and wing premotor control networks in *Drosophila. Nature*, 10.1038/s41586-024-07600-z. https://doi.org/10.1038/s41586-024-07600-z

[22] Cheong, H.S.J., Eichler, K., Stürner, T., Asinof, S.K., Champion, A.S., Marin, E.C., Oram, T.B., Sumathipala, M., Venkatasubramanian, L., Namiki, S., et al. (2024). Transforming descending input into behavior: The organization of premotor circuits in the Drosophila Male Adult Nerve Cord connectome *eLife 13*:RP96084. https://doi.org/10.7554/eLife.96084.1

[23] Pearson, K. G. (1972). Central programming and reflex control of walking in the cockroach. *Journal of Experimental Biology*, **56**, 173–193.

[24] Bässler, U., & Wagner, U. (1983). Motor output of the denervated thoracic ventral nerve cord in the stick insect *Carausius morosus*. *Journal of Experimental Biology*, **105**, 127–145.

[25] Büschges A. Inhibitory synaptic drive patterns motoneuronal activity in rhythmic preparations of isolated thoracic ganglia in the stick insect. Brain Res. 1998 Feb 9;783(2):262-71. doi: 10.1016/s0006-8993(97)01370-x.

[26] Büschges A, Manira AE. Sensory pathways and their modulation in the control of locomotion. Curr Opin Neurobiol. 1998 Dec;8(6):733-9. doi: 10.1016/s0959-4388(98)80115-3.

[27] Mantziaris C, Bockemühl T, Büschges A. Central pattern generating networks in insect locomotion. Dev Neurobiol. 2020 Jan;80(1-2):16-30. doi: 10.1002/dneu.22738. Epub 2020 Mar 23. PMID: 32128970.

[28] Büschges A. Sensory control and organization of neural networks mediating coordination of multisegmental organs for locomotion. J Neurophysiol. 2005 Mar;93(3):1127-35. doi: 10.1152/jn.00615.2004.

[29] Ritzmann RE, Büschges A. Adaptive motor behavior in insects. Curr Opin Neurobiol. 2007 Dec;17(6):629-36. doi: 10.1016/j.conb.2008.01.001.

[30] Büschges A, Scholz H, El Manira A. New moves in motor control. Curr Biol. 2011 Jul 12;21(13):R513-24. doi: 10.1016/j.cub.2011.05.029.

[31] Marder E, Bucher D. Central pattern generators and the control of rhythmic movements. Curr Biol. 2001 Nov 27;11(23):R986-96. doi: 10.1016/s0960-9822(01)00581-4.

[32] Marder E, Kedia S, Morozova EO. New insights from small rhythmic circuits. Curr Opin Neurobiol. 2022 Oct;76:102610. doi: 10.1016/j.conb.2022.102610. Epub 2022 Aug 17.

[33] Calabrese RL, Marder E. Degenerate neuronal and circuit mechanisms important for generating rhythmic motor patterns. Physiol Rev. 2025 Jan 1;105(1):95-135. doi: 10.1152/physrev.00003.2024. Epub 2024 Jun 13. PMID: 39453990.

[34] Heckscher ES, Lockery SR, Doe CQ. Characterization of Drosophila larval crawling at the level of organism, segment, and somatic body wall musculature. J Neurosci. 2012 Sep 5;32(36):12460-71. doi: 10.1523/JNEUROSCI.0222-12.2012.

[35] Gjorgjieva J, Berni J, Evers JF, Eglen SJ. Neural circuits for peristaltic wave propagation in crawling Drosophila larvae: analysis and modeling. Front Comput Neurosci. 2013 Apr 4;7:24. doi: 10.3389/fncom.2013.00024.

[36] Kohsaka H, Takasu E, Morimoto T, Nose A. A group of segmental premotor interneurons regulates the speed of axial locomotion in Drosophila larvae. Curr Biol. 2014 Nov 17;24(22):2632-42. doi: 10.1016/j.cub.2014.09.026. Epub 2014 Oct 16. PMID: 25438948.

[37] Pulver SR, Bayley TG, Taylor AL, Berni J, Bate M, Hedwig B. Imaging fictive locomotor patterns in larval Drosophila. J Neurophysiol. 2015 Nov;114(5):2564-77. doi: 10.1152/jn.00731.2015. Epub 2015 Aug 26. PMID: 26311188; PMCID: PMC4637366.

[38] Fushiki A, Zwart MF, Kohsaka H, Fetter RD, Cardona A, Nose A. A circuit mechanism for the propagation of waves of muscle contraction in Drosophila. Elife. 2016 Feb 15;5:e13253. doi: 10.7554/eLife.13253.

[39] Zarin AA, Mark B, Cardona A, Litwin-Kumar A, Doe CQ. A multilayer circuit architecture for the generation of distinct locomotor behaviors in *Drosophila*. Elife. 2019 Dec 23;8:e51781. doi: 10.7554/eLife.51781. PMID: 31868582; PMCID: PMC6994239.

[40] Lacin, H., Chen, H. M., Long, X., Singer, R. H., Lee, T., & Truman, J. W. (2019). Neurotransmitter identity is acquired in a lineage-restricted manner in the *Drosophila* CNS. *eLife, 8*, e43701. https://doi.org/10.7554/eLife.43701

[41] Harris, R. M., Pfeiffer, B. D., Rubin, G. M., & Truman, J. W. (2015). Neuron hemilineages provide the functional ground plan for the Drosophila ventral nervous system. *eLife, 4*, e04493. https://doi.org/10.7554/eLife.04493

[42] Soffers JHM, Beck E, Sytkowski DJ, Maughan ME, Devarakonda D, Zhu Y, Wilson BA, Chen YD, Erclik T, Truman JW, Skeath JB, Lacin H. A library of lineage-specific driver lines connects developing neuronal circuits to behavior in the *Drosophila* ventral nerve cord. Elife. 2025 Jun 10;14:RP106042. doi: 10.7554/eLife.106042.

[43] Gowda SBM, Banu A, Hussain S, Mohammad F. Neuronal mechanisms regulating locomotion in adult Drosophila. J Neurosci Res. 2024 Apr;102(4):e25332. doi: 10.1002/jnr.25332. PMID: 38646942.

[44] Mendes, C. S., Bartos, I., Akay, T., Márka, S., & Mann, R. S. (2013). Quantification of gait parameters in freely walking wild type and sensory deprived Drosophila melanogaster. *eLife*, *2*, e00231. https://doi.org/10.7554/eLife.00231

[45] Tuthill, J. C., & Azim, E. (2018). Proprioception. *Current biology : CB*, *28*(5), R194–R203. https://doi.org/10.1016/j.cub.2018.01.064

[46] Chockley, A. S., Dinges, G. F., Di Cristina, G., Ratican, S., Bockemühl, T., & Büschges, A. (2022). Subsets of leg proprioceptors influence leg kinematics but not interleg coordination in Drosophila melanogaster walking. *The Journal of experimental biology*, *225*(20), jeb244245. https://doi.org/10.1242/jeb.244245

[47] Lee S.J. , Dallmann C.J. , Cook A., Tuthill J.C. , Agrawal S. (2025). Divergent neural circuits for proprioceptive and exteroceptive sensing of the *Drosophila* leg. *Nature Comm.* 16, 4105; doi: https://doi.org/10.1038/s41467-025-59302-3

[48] Bernstein N. (1967). The co-ordination and regulation of movements. *Oxford: Pergamon*

[49] Bizzi, E., and Cheung, V. C. (2013). The neural origin of muscle synergies. *Frontiers in computational neuroscience*, *7*, 51. https://doi.org/10.3389/fncom.2013.00051

[50] Sherrington C. S. (1892). Notes on the Arrangement of some Motor Fibres in the Lumbo-Sacral Plexus. *The Journal of physiology*, *13*(6), 621–772.17. https://doi.org/10.1113/jphysiol.1892.sp000428

[51] Sharrard W. J. (1964). The segmental innervation of the lower limb muscles in man. *Annals of the Royal College of Surgeons of England*, *35*(2), 106–122

[52] Ferrier D. and Yeo G. F. (1881). The functional relations of the motor roots of the brachial and lumbo-sacral plexuses. *Proceedings of the Royal Society of London*, vol. 32, no. 212-215.

[53] Bizzi, E., Mussa-Ivaldi, F. A., & Giszter, S. (1991). Computations underlying the execution of movement: a biological perspective. *Science*, *253*(5017), 287–291. https://doi.org/10.1126/science.1857964

[54] Giszter, S. F., Mussa-Ivaldi, F. A., & Bizzi, E. (1993). Convergent force fields organized in the frog's spinal cord. *The Journal of neuroscience : the official journal of the Society for Neuroscience*, *13*(2), 467–491. https://doi.org/10.1523/JNEUROSCI.13-02-00467.1993

[55] Lemay, M. A., & Grill, W. M. (2004). Modularity of motor output evoked by intraspinal microstimulation in cats. *Journal of neurophysiology*, *91*(1), 502–514. https://doi.org/10.1152/jn.00235.2003

[56] Mussa-Ivaldi, F. A., Giszter, S. F., & Bizzi, E. (1994). Linear combinations of primitives in vertebrate motor control. *Proceedings of the National Academy of Sciences*, *91*(16), 7534–7538. https://doi.org/10.1073/pnas.91.16.7534

[57] Kargo, W. J., & Giszter, S. F. (2000). Rapid correction of aimed movements by summation of force-field primitives. *The Journal of neuroscience*, *20*(1), 409–426. https://doi.org/10.1523/JNEUROSCI.20-01-00409.2000

[58] Lemay, M. A., Galagan, J. E., Hogan, N., & Bizzi, E. (2001). Modulation and vectorial summation of the spinalized frog's hindlimb end-point force produced by intraspinal electrical stimulation of the cord. *IEEE transactions on neural systems and rehabilitation engineering 9*(1), 12–23. https://doi.org/10.1109/7333.918272

[59] Maier, M. A., & Hepp-Reymond, M. C. (1995). EMG activation patterns during force production in precision grip. II. Muscular synergies in the spatial and temporal domain. *Experimental brain research*, *103*(1), 123–136. https://doi.org/10.1007/BF00241970

[60] Huesler, E. J., Maier, M. A., & Hepp-Reymond, M. C. (2000). EMG activation patterns during force production in precision grip. III. Synchronisation of single motor units. *Experimental brain research*, *134*(4), 441–455. https://doi.org/10.1007/s002210000484

[61] Ivanenko, Y. P., Grasso, R., Zago, M., Molinari, M., Scivoletto, G., Castellano, V., Macellari, V., & Lacquaniti, F. (2003). Temporal components of the motor patterns expressed by the human spinal cord reflect foot kinematics. *Journal of neurophysiology*, *90*(5), 3555–3565. https://doi.org/10.1152/jn.00223.2003

[62] Hart, C. B., & Giszter, S. F. (2004). Modular premotor drives and unit bursts as primitives for frog motor behaviors. *The Journal of neuroscience*, *24*(22), 5269–5282. https://doi.org/10.1523/JNEUROSCI.5626-03.2004

[63] Yakovenko, S., Krouchev, N., & Drew, T. (2011). Sequential activation of motor cortical neurons contributes to intralimb coordination during reaching in the cat by modulating muscle synergies. *Journal of neurophysiology*, *105*(1), 388–409. https://doi.org/10.1152/jn.00469.2010

[64] Overduin, S. A., d'Avella, A., Carmena, J. M., & Bizzi, E. (2012). Microstimulation activates a handful of muscle synergies. *Neuron*, *76*(6), 1071–1077. https://doi.org/10.1016/j.neuron.2012.10.018

[65] Singh, R. E., Iqbal, K., White, G., & Hutchinson, T. E. (2018). A Systematic Review on Muscle Synergies: From Building Blocks of Motor Behavior to a Neurorehabilitation Tool. *Applied bionics and biomechanics*, *2018*, 3615368. https://doi.org/10.1155/2018/3615368

[66] Kutch, J. J., & Valero-Cuevas, F. J. (2012). Challenges and new approaches to proving the existence of muscle synergies of neural origin. *PLoS computational biology*, *8*(5), e1002434. https://doi.org/10.1371/journal.pcbi.1002434

[67] Capaday, C., & van Vreeswijk, C. (2015). Linear summation of outputs in a balanced network model of motor cortex. *Frontiers in computational neuroscience*, *9*, 63. https://doi.org/10.3389/fncom.2015.00063

[68] Romanes G. J. (1951). The motor cell columns of the lumbo-sacral spinal cord of the cat. *The Journal of comparative neurology*, *94*(2), 313–363. https://doi.org/10.1002/cne.900940209

[69] Cruce W. L. (1974). The anatomical organization of hindlimb motoneurons in the lumbar spinal cord of the frog, Rana catesbiana. *The Journal of comparative neurology*, *153*(1), 59–76. https://doi.org/10.1002/cne.901530106

[70] Tsuchida, T., Ensini, M., Morton, S. B., Baldassare, M., Edlund, T., Jessell, T. M., & Pfaff, S. L. (1994). Topographic organization of embryonic motor neurons defined by expression of LIM homeobox genes. *Cell*, *79*(6), 957–970. https://doi.org/10.1016/0092-8674(94)90027-2

[71] Lanuza, G. M., Gosgnach, S., Pierani, A., Jessell, T. M., & Goulding, M. (2004). Genetic identification of spinal interneurons that coordinate left-right locomotor activity necessary for walking movements. *Neuron*, *42*(3), 375–386. https://doi.org/10.1016/s0896-6273(04)00249-1

[72] Bellardita, C., & Kiehn, O. (2015). Phenotypic characterization of speed-associated gait changes in mice reveals modular organization of locomotor networks. *Current biology : CB*, *25*(11), 1426–1436. https://doi.org/10.1016/j.cub.2015.04.005

[73] Sengupta, M., Daliparthi, V., Roussel, Y., Bui, T. V., & Bagnall, M. W. (2021). Spinal V1 neurons inhibit motor targets locally and sensory targets distally. *Current biology : CB*, *31*(17), 3820–3833.e4. https://doi.org/10.1016/j.cub.2021.06.053

[74] Yang, W., Kanodia, H., & Arber, S. (2023). Structural and functional map for forelimb movement phases between cortex and medulla. *Cell*, *186*(1), 162–177.e18. https://doi.org/10.1016/j.cell.2022.12.009

[75] Berkowitz A, Laurent G. Local control of leg movements and motor patterns during grooming in locusts. J Neurosci. 1996 Dec 15;16(24):8067-78. doi: 10.1523/JNEUROSCI.16-24-08067.1996.

[76] Zill SN, Chaudhry S, Büschges A, Schmitz J. Force feedback reinforces muscle synergies in insect legs. Arthropod Struct Dev. 2015 Nov;44(6 Pt A):541-53. doi: 10.1016/j.asd.2015.07.001.

[77] Zill SN, Dallmann CJ, Büschges A, Chaudhry S, Schmitz J. Force dynamics and synergist muscle activation in stick insects: the effects of using joint torques as mechanical stimuli. J Neurophysiol. 2018 Oct 1;120(4):1807-1823. doi: 10.1152/jn.00371.2018.

[78] Sponberg S, Daniel TL, Fairhall AL. Dual dimensionality reduction reveals independent encoding of motor features in a muscle synergy for insect flight control. PLoS Comput Biol. 2015 Apr 28;11(4):e1004168. doi: 10.1371/journal.pcbi.1004168.

[79] Ruthe A, Mantziaris C, Büschges A. The synaptic drive of central pattern-generating networks to leg motor neurons of a walking insect is motor neuron pool specific. Curr Biol. 2024 Feb 26;34(4):910-915.e2. doi: 10.1016/j.cub.2024.01.026.

[80] Gowda, S. B. M., Paranjpe, P. D., Reddy, O. V., Thiagarajan, D., Palliyil, S., Reichert, H., & VijayRaghavan, K. (2018). GABAergic inhibition of leg motoneurons is required for normal walking behavior in freely moving *Drosophila*. *Proceedings of the National Academy of Sciences of the United States of America*, *115*(9), E2115–E2124. https://doi.org/10.1073/pnas.1713869115

[81] Shepherd, D., Harris, R., Williams, D. W., & Truman, J. W. (2016). Postembryonic lineages of the Drosophila ventral nervous system: Neuroglian expression reveals the adult hemilineage associated fiber tracts in the adult thoracic neuromeres. *The Journal of comparative neurology*, *524*(13), 2677–2695. https://doi.org/10.1002/cne.23988

[82] Truman, J. W., Schuppe, H., Shepherd, D., & Williams, D. W. (2004). Developmental architecture of adult-specific lineages in the ventral CNS of Drosophila. *Development*, *131*(20), 5167–5184. https://doi.org/10.1242/dev.01371

[83] Birkholz, O., Rickert, C., Nowak, J., Coban, I. C., & Technau, G. M. (2015). Bridging the gap between postembryonic cell lineages and identified embryonic neuroblasts in the ventral nerve cord of Drosophila melanogaster. *Biology open*, *4*(4), 420–434. https://doi.org/10.1242/bio.201411072

[84] Lacin, H., & Truman, J. W. (2016). Lineage mapping identifies molecular and architectural similarities between the larval and adult Drosophila central nervous system. *eLife*, *5*, e13399. https://doi.org/10.7554/eLife.13399

[85] Marin, E. C., Morris B. J., Stürner T., Champion A.S., Krzeminski D., Badalamente G., Gkantia M., Dunne C. R., Eichler K., Takemura S., et al. (2024). Systematic annotation of a complete adult male *Drosophila* nerve cord connectome reveals principles of functional organisation. eLife 13:RP97766. https://doi.org/10.7554/eLife.97766.1

[86] Costa, M., Manton, J. D., Ostrovsky, A. D., Prohaska, S., & Jefferis, G. S. (2016). NBLAST: Rapid, Sensitive Comparison of Neuronal Structure and Construction of Neuron Family Databases. *Neuron*, *91*(2), 293–311. https://doi.org/10.1016/j.neuron.2016.06.012

[87] Mamiya, A., Gurung, P., & Tuthill, J. C. (2018). Neural Coding of Leg Proprioception in Drosophila. *Neuron*, *100*(3), 636–650.e6. https://doi.org/10.1016/j.neuron.2018.09.009

[88] Agrawal, S., Dickinson, E. S., Sustar, A., Gurung, P., Shepherd, D., Truman, J. W., & Tuthill, J. C. (2020). Central processing of leg proprioception in *Drosophila*. *eLife*, *9*, e60299. https://doi.org/10.7554/eLife.60299

[89] Chen, C., Agrawal, S., Mark, B., Mamiya, A., Sustar, A., Phelps, J. S., Lee, W. A., Dickson, B. J., Card, G. M., & Tuthill, J. C. (2021). Functional architecture of neural circuits for leg proprioception in Drosophila. *Current biology : CB*, *31*(23), 5163–5175.e7. https://doi.org/10.1016/j.cub.2021.09.035

[90] Mathis, A., Mamidanna, P., Cury, K. M., Abe, T., Murthy, V. N., Mathis, M. W., & Bethge, M. (2018). DeepLabCut: markerless pose estimation of user-defined body parts with deep learning. *Nature neuroscience*, *21*(9), 1281–1289. https://doi.org/10.1038/s41593-018-0209-y

[91] Schilling M, Cruse H. neuroWalknet, a controller for hexapod walking allowing for context dependent behavior. PLoS Comput Biol. 2023 Jan 24;19(1):e1010136. doi: 10.1371/journal.pcbi.1010136.

[92] Jovanic, T., Schneider-Mizell, C. M., Shao, M., Masson, J. B., Denisov, G., Fetter, R. D., Mensh, B. D., Truman, J. W., Cardona, A., & Zlatic, M. (2016). Competitive Disinhibition Mediates Behavioral Choice and Sequences in Drosophila. *Cell*, *167*(3), 858–870.e19. https://doi.org/10.1016/j.cell.2016.09.009

[93] Chevalier, G., & Deniau, J. M. (1990). Disinhibition as a basic process in the expression of striatal functions. *Trends in neurosciences*, *13*(7), 277–280. https://doi.org/10.1016/0166-2236(90)90109-n

[94] Mink J. W. (1996). The basal ganglia: focused selection and inhibition of competing motor programs. *Progress in neurobiology*, *50*(4), 381–425. https://doi.org/10.1016/s0301-0082(96)00042-1

[95] Grillner, S., Hellgren, J., Ménard, A., Saitoh, K., & Wikström, M. A. (2005). Mechanisms for selection of basic motor programs--roles for the striatum and pallidum. *Trends in neurosciences*, *28*(7), 364–370. https://doi.org/10.1016/j.tins.2005.05.004

[96] Benjamin, P. R., Staras, K., & Kemenes, G. (2010). What roles do tonic inhibition and disinhibition play in the control of motor programs?. *Frontiers in behavioral neuroscience*, *4*, 30. https://doi.org/10.3389/fnbeh.2010.00030

[97] Zhu J., Boivin J., Garner A., Ning J., Zhao Y. Q., Ohyama T. (2024) Feedback inhibition by a descending GABAergic neuron regulates timing of escape behavior in Drosophila larvae. *eLife 13*:RP93978 https://doi.org/10.7554/eLife.93978.1

[98] Zhao, W., Zhou, P., Gong, C., Ouyang, Z., Wang, J., Zheng, N., & Gong, Z. (2019). A disinhibitory mechanism biases Drosophila innate light preference. *Nature communications*, *10*(1), 124. https://doi.org/10.1038/s41467-018-07929-w

[99] Zwart MF, Pulver SR, Truman JW, Fushiki A, Fetter RD, Cardona A, Landgraf M. Selective Inhibition Mediates the Sequential Recruitment of Motor Pools. Neuron. 2016 Aug 3;91(3):615-28. doi: 10.1016/j.neuron.2016.06.031

[100] Kiehn O. (2016). Decoding the organization of spinal circuits that control locomotion. *Nature reviews. Neuroscience*, *17*(4), 224–238.

[101] Talpalar, A. E., Endo, T., Löw, P., Borgius, L., Hägglund, M., Dougherty, K. J., Ryge, J., Hnasko, T. S., & Kiehn, O. (2011). Identification of minimal neuronal networks involved in flexor-extensor alternation in the mammalian spinal cord. *Neuron*, *71*(6), 1071–1084. https://doi.org/10.1016/j.neuron.2011.07.011

[102] Cowley, K. C., & Schmidt, B. J. (1995). Effects of inhibitory amino acid antagonists on reciprocal inhibitory interactions during rhythmic motor activity in the in vitro neonatal rat spinal cord. *Journal of neurophysiology*, *74*(3), 1109–1117. https://doi.org/10.1152/jn.1995.74.3.1109

[103] Kjaerulff, O., & Kiehn, O. (1997). Crossed rhythmic synaptic input to motoneurons during selective activation of the contralateral spinal locomotor network. *The Journal of neuroscience,17*(24), 9433–9447. https://doi.org/10.1523/JNEUROSCI.17-24-09433.1997

[104] Whelan, P., Bonnot, A., & O'Donovan, M. J. (2000). Properties of rhythmic activity generated by the isolated spinal cord of the neonatal mouse. *Journal of neurophysiology*, *84*(6), 2821–2833. https://doi.org/10.1152/jn.2000.84.6.2821

[105] Endo, T., & Kiehn, O. (2008). Asymmetric operation of the locomotor central pattern generator in the neonatal mouse spinal cord. *Journal of neurophysiology*, *100*(6), 3043–3054. https://doi.org/10.1152/jn.90729.2008

[106] Zhang, J., Lanuza, G. M., Britz, O., Wang, Z., Siembab, V. C., Zhang, Y., Velasquez, T., Alvarez, F. J., Frank, E., & Goulding, M. (2014). V1 and v2b interneurons secure the alternating flexor-extensor motor activity mice require for limbed locomotion. *Neuron*, *82*(1), 138–150. https://doi.org/10.1016/j.neuron.2014.02.013

[107] Büschges, A. (1995). Role of local nonspiking interneurons in the generation of rhythmic motor activity in the stick insect. *Journal of Neurobiology*, **27**, 488–512.

[108] Ryckebusch S, Laurent G. Rhythmic patterns evoked in locust leg motor neurons by the muscarinic agonist pilocarpine. J Neurophysiol. 1993 May;69(5):1583-95. doi: 10.1152/jn.1993.69.5.1583. PMID: 8389831.

[109] Dallmann, C. J., Luo, Y., Agrawal, S., Chou, G. M., Cook, A., Brunton, B. W., & Tuthill, J. C. (2024). Presynaptic inhibition selectively suppresses leg proprioception in behaving *Drosophila*. *bioRxiv : the preprint server for biology*, 2023.10.20.563322. https://doi.org/10.1101/2023.10.20.563322

[110] Sherrington, C. S., (1910), Flexion-reflex of the limb, crossed extension-reflex, and reflex stepping and standing. *The Journal of Physiology*, 40 doi: 10.1113/jphysiol.1910.sp001362

[111] Andersson O, Grillner S (1983). Peripheral control of the cat's step cycle. II Entrainment of the central pattern generators for locomotion by sinusoidal hip movements during "fictive locomotion". Acta Physiol Sc. 118:229-239

[112] Field L. H., Burrows M. (1982). Reflex effects of the femoral chordotonal organ upon leg motor neurones of the Locust. *J Exp Biol.,* 101 (1): 265–285. https://doi.org/10.1242/jeb.101.1.265

[113] Kriellaars, D. J., Brownstone, R. M., Noga, B. R., & Jordan, L. M. (1994). Mechanical entrainment of fictive locomotion in the decerebrate cat. *Journal of neurophysiology*, *71*(6), 2074–2086. https://doi.org/10.1152/jn.1994.71.6.2074

[114] Pearson K. G. (2004). Generating the walking gait: role of sensory feedback. *Progress in brain research*, *143*, 123–129. https://doi.org/10.1016/S0079-6123(03)43012-4

[115] Marlot, D., Macron, J. M., & Duron, B. (1987). Inhibitory and excitatory effects on respiration by phrenic nerve afferent stimulation in cats. *Respiration physiology*, *69*(3), 321–333. https://doi.org/10.1016/0034-5687(87)90086-7

[116] Jammes, Y., Buchler, B., Delpierre, S., Rasidakis, A., Grimaud, C., & Roussos, C. (1986). Phrenic afferents and their role in inspiratory control. *Journal of applied physiology (Bethesda, Md. : 1985)*, *60*(3), 854–860. https://doi.org/10.1152/jappl.1986.60.3.854

[117] Brown, T. G. (1911). The intrinsic factors in the act of progression in the mammal. Proceedings of the Royal Society of London. Series B, containing papers of a biological character, 84(572), 308-319.

[118] Brown T. G. (1914). On the nature of the fundamental activity of the nervous centres; together with an analysis of the conditioning of rhythmic activity in progression, and a theory of the evolution of function in the nervous system. *The Journal of physiology*, *48*(1), 18–46. https://doi.org/10.1113/jphysiol.1914.sp001646

[119] Stuart, D. G., & Hultborn, H. (2008). Thomas Graham Brown (1882--1965), Anders Lundberg (1920-), and the neural control of stepping. *Brain research reviews*, *59*(1), 74–95. https://doi.org/10.1016/j.brainresrev.2008.06.001

[120] Zakotnik J, Matheson T, Dürr V. Co-contraction and passive forces facilitate load compensation of aimed limb movements. J Neurosci. 2006 May 10;26(19):4995-5007. doi: 10.1523/JNEUROSCI.0161-06.2006.

[121] Günzel Y, Schmitz J, Dürr V. Locomotor resilience through load-dependent modulation of muscle co-contraction. J Exp Biol. 2022 Sep 15;225(18):jeb244361. doi: 10.1242/jeb.244361.

[122] Ogawa S, Yamawaki Y. Timing of the co-activation of antagonist muscles affects foreleg movements during mantis strikes. J Insect Physiol. 2025 Mar;161:104753. doi: 10.1016/j.jinsphys.2025.104753.

[123] Duysens, J., De Groote, F., & Jonkers, I. (2013). The flexion synergy, mother of all synergies and father of new models of gait. *Frontiers in computational neuroscience*, *7*, 14. https://doi.org/10.3389/fncom.2013.00014

[124] Zhong, G., Shevtsova, N. A., Rybak, I. A., & Harris-Warrick, R. M. (2012). Neuronal activity in the isolated mouse spinal cord during spontaneous deletions in fictive locomotion: insights into locomotor central pattern generator organization. *The Journal of physiology*, *590*(19), 4735–4759. https://doi.org/10.1113/jphysiol.2012.240895

[125] Heitler, W. J. (1974). The locust jump—Specialisations of the metathoracic femoral-tibial joint. *Journal of Comparative Physiology*, 89(1), 93–104. https://doi.org/10.1007/BF00696166

[126] Bennet-Clark, H. C. (1975). The energetics of the jump of the locust Schistocerca gregaria. *Journal of Experimental Biology*, 63(1), 53–83. https://journals.biologists.com/jeb/article/63/1/53/22130/The-energetics-of-the-jump-of-the-locust

[127] Page, W. R., & Burrows, M. (2008). Motor control of aimed limb movements in an insect. *Journal of Neurophysiology*, 100(5), 2682–2694. https://journals.physiology.org/doi/full/10.1152/jn.00922.2007

[128] Hooper SL, Guschlbauer C, Blümel M, Rosenbaum P, Gruhn M, Akay T, Büschges A. Neural control of unloaded leg posture and of leg swing in stick insect, cockroach, and mouse differs from that in larger animals. J Neurosci. 2009 Apr 1;29(13):4109-19. doi: 10.1523/JNEUROSCI.5510-08.2009.

[129] Hampel S, Franconville R, Simpson JH, Seeds AM. A neural command circuit for grooming movement control. Elife. 2015 Sep 7;4:e08758. doi: 10.7554/eLife.08758. PMID: 26344548; PMCID: PMC4599031.

[130] Landgraf M, Jeffrey V, Fujioka M, Jaynes JB, Bate M. Embryonic origins of a motor system: motor dendrites form a myotopic map in Drosophila. PLoS Biol. 2003 Nov;1(2):E41. doi: 10.1371/journal.pbio.0000041

[131] Vosshall LB, Wong AM, Axel R. An olfactory sensory map in the fly brain. Cell. 2000 Jul 21;102(2):147-59. doi: 10.1016/s0092-8674(00)00021-0

[132] Wong AM, Wang JW, Axel R. Spatial representation of the glomerular map in the Drosophila protocerebrum. Cell. 2002 Apr 19;109(2):229-41. doi: 10.1016/s0092-8674(02)00707-9

[133] Gao Q, Yuan B, Chess A. Convergent projections of Drosophila olfactory neurons to specific glomeruli in the antennal lobe. Nat Neurosci. 2000 Aug;3(8):780-5. doi: 10.1038/77680

[134] Mamiya A, Sustar A, Siwanowicz I, Qi Y, Lu TC, Gurung P, Chen C, Phelps JS, Kuan AT, Pacureanu A, Lee WA, Li H, Mhatre N, Tuthill JC. Biomechanical origins of proprioceptor feature selectivity and topographic maps in the Drosophila leg. Neuron. 2023 Oct 18;111(20):3230-3243.e14. doi: 10.1016/j.neuron.2023.07.009

[135] McLean DL, Fan J, Higashijima S, Hale ME, Fetcho JR. A topographic map of recruitment in spinal cord. Nature. 2007 Mar 1;446(7131):71-5. doi: 10.1038/nature05588

[136] Gatto G, Bourane S, Ren X, Di Costanzo S, Fenton PK, Halder P, Seal RP, Goulding MD. A Functional Topographic Map for Spinal Sensorimotor Reflexes. Neuron. 2021 Jan 6;109(1):91-104.e5. doi: 10.1016/j.neuron.2020.10.003

[137] Lobato-Rios V, Ramalingasetty ST, Özdil PG, Arreguit J, Ijspeert AJ, Ramdya P. NeuroMechFly, a neuromechanical model of adult Drosophila melanogaster. Nat Methods. 2022 May;19(5):620-627. doi: 10.1038/s41592-022-01466-7.

[138] Wang-Chen S, Stimpfling VA, Lam TKC, Özdil PG, Genoud L, Hurtak F, Ramdya P. NeuroMechFly v2: simulating embodied sensorimotor control in adult Drosophila. Nat Methods. 2024 Dec;21(12):2353-2362. doi: 10.1038/s41592-024-02497-y.

[139] Karashchuk L, Li JS, Chou GM, Walling-Bell S, Brunton SL, Tuthill JC, Brunton BW. Sensorimotor delays constrain robust locomotion in a 3D kinematic model of fly walking. Elife. 2025 May 15;13:RP99005. doi: 10.7554/eLife.99005. PMID: 40372779; PMCID: PMC12081000.

[140] Jenett, A., Rubin, G. M., Ngo, T. T., Shepherd, D., Murphy, C., Dionne, H., Pfeiffer, B. D., Cavallaro, A., Hall, D., Jeter, J.,et al., (2012). A GAL4-driver line resource for Drosophila neurobiology. *Cell reports*, *2*(4), 991–1001. https://doi.org/10.1016/j.celrep.2012.09.011

[141] Ravbar, P., Branson, K., & Simpson, J. H. (2019). An automatic behavior recognition system classifies animal behaviors using movements and their temporal context. *Journal of neuroscience methods*, *326*, 108352. https://doi.org/10.1016/j.jneumeth.2019.108352

[142] Court, R., Namiki, S., Armstrong, J. D., Börner, J., Card, G., Costa, M., Dickinson, M., Duch, C., Korff, W., Mann, R., Merritt, D., Murphey, R. K., Seeds, A. M., Shirangi, T., Simpson, J. H., Truman, J. W., Tuthill, J. C., Williams, D. W., & Shepherd, D. (2020). A Systematic Nomenclature for the Drosophila Ventral Nerve Cord. *Neuron*, *107*(6), 1071–1079.e2. https://doi.org/10.1016/j.neuron.2020.08.005

[143] Saalfeld, S., Cardona, A., Hartenstein, V., & Tomancak, P. (2009). CATMAID: collaborative annotation toolkit for massive amounts of image data. *Bioinformatics*, *25*(15), 1984–1986. https://doi.org/10.1093/bioinformatics/btp266

[144] Maitin-Shepard, J. et al. (2021) google/neuroglancer: Zenodo https://doi.org/10.5281/zenodo.5573294